Laminar Neural Dynamics of Auditory Evoked Responses: Computational Modeling of Local Field Potentials in Auditory Cortex of Non-Human Primates

Vincent S.C. Chien[1,2,3], Peng Wang[1,4,5], Burkhard Maess[1], Yonatan Fishman[6], Thomas R. Knösche[1]

[1] Max Planck Institute for Human Cognitive and Brain Sciences, Germany

[2] Translational Imaging Research Center, Taipei Medical University Hospital, Taiwan

[3] Neuroscience Research Center, Taipei Medical University, Taiwan

[4] Institute of Psychology, University of Greifswald, Germany

[5] Institute of Psychology, University of Regensburg, Germany

[6] Departments of Neurology and Neuroscience, Albert Einstein College of Medicine, USA

Abstract

Evoked neural responses to sensory stimuli have been extensively investigated in humans and animal models both to enhance our understanding of brain function and to aid in clinical diagnosis of neurological and neuropsychiatric conditions. Recording and imaging techniques such as electroencephalography (EEG), magnetoencephalography (MEG), local field potentials (LFPs), and calcium imaging provide complementary information about different aspects of brain activity at different spatial and temporal scales. Modeling and simulations provide a way to integrate these different types of information to clarify underlying neural mechanisms.

In this study, we aimed to shed light on the neural dynamics underlying auditory evoked responses by fitting a rate-based model to LFPs recorded via multi-contact electrodes which simultaneously sampled neural activity across cortical laminae. Recordings included neural population responses to best-frequency (BF) and non-BF tones at four representative sites in primary auditory cortex (A1) of awake monkeys. The model considered major neural populations of excitatory, parvalbumin-expressing (PV), and somatostatin-expressing (SOM) neurons across layers 2/3, 4, and 5/6. Unknown parameters, including the connection strength between the populations, were fitted to the data. Our results revealed similar population dynamics, fitted model parameters, predicted equivalent current dipoles (ECD), tuning curves, and lateral inhibition profiles across recording sites and animals, in spite of quite different extracellular current distributions. We found that PV firing rates were higher in BF than in non-BF responses, mainly due to different strengths of tonotopic thalamic input, whereas SOM firing rates were higher in non-BF than in BF responses due to lateral inhibition.

In conclusion, we demonstrate the feasibility of the model-fitting approach in identifying the contributions of cell-type specific population activity to stimulus-evoked LFPs across cortical laminae, providing a foundation for further investigations into the dynamics of neural circuits underlying cortical sensory processing.

***keywords**:* auditory processing, cortical microcircuits, lateral inhibition, neural mass model

1 Introduction

Neural responses to sensory stimuli have been extensively studied in order to elucidate how the brain represents features of the environment. Evoked responses are a specific kind of *event-related* signal that reflect (mostly electrical) brain activity in response to stimuli, such as tactile impulses, images, or sounds. In humans, cortical evoked responses can be recorded noninvasively via electroencephalography (EEG) and magnetoencephalography (MEG), which are widely used methodologies for probing brain function in health and disease. In order to draw valid and informative conclusions from these noninvasively recorded signals, it is important to understand the neural mechanisms underlying their generation. The cortical sources of EEG and MEG are thought to be intracellular currents primarily associated with postsynaptic potentials in pyramidal neurons (Lopes da Silva, 2013; Næss et al., 2021; Vaughan H.G.Jr, 1988). Pyramidal neurons and interneurons constitute multiple distinct populations in different layers of the cortex, which are locally and globally interconnected in a recurrent fashion. Already at the local level, these recurrent networks implement important functions (e.g., Chien et al., 2019; Hahn et al., 2022; Kunze et al., 2019). In order to eventually map the observed evoked responses onto these functions, it is crucial to obtain detailed information about how various neuronal cell types and synaptic connections contribute to their generation.

Invasive studies in animal models can contribute substantially to this aim by allowing the recording/imaging of layer-specific local field potentials (LFP) and cell-type specific neural firing (see Sections 1.1 and 1.2). Such animal model studies have already provided considerable information about lamina-specific neural activity (Bruyns-Haylett et al., 2017; Hajizadeh et al., 2019, 2021, 2022; Kohl et al., 2022; Neymotin et al., 2020; Sumner et al., 2021) and enhanced our understanding of the

functional roles of various types of inhibitory interneurons in cortical processing (Aponte et al., 2021; Blackwell & Geffen, 2017; Liu et al., 2019; Liu & Kanold, 2021; Studer & Barkat, 2022). However, to more thoroughly elucidate the underlying neural generators of evoked responses and their relationship with information processing in the brain, it is necessary to mechanistically link together the available information about cell types and local neuronal circuits in the brain, intracranially-recorded LFPs, and extracranially-measured EEG and MEG signals. This task requires computational models. Although several efforts in this direction have been made (see Section 1.3), most modeling studies, such as spiking-based single-column models or rate-based multi-column models, are limited by being purely forward simulations without fitting the models to actual recordings of brain activity (e.g., LFPs and EEG/MEG), leaving their proposed theories less mechanistically and empirically grounded.

1.1 Layer-specific data - local field potentials

Linear-array multi-channel electrodes are a unique methodological tool which allows the simultaneous recording of LPFs across cortical layers (e.g., Fishman et al., 2001; Schroeder et al., 1998; Steinschneider et al., 2003). The high spatial resolution of LFPs provides valuable information regarding the intracranial generators of event-related potentials/fields (ERPs/ERFs) and information flow within and across cortical layers. Multi-unit activity (MUA), which can be extracted from high-frequency components of LFPs, reflects the spiking of local neuron populations in the vicinity of each electrode contact. Current source density (CSD), the second spatial derivative of the LFPs, provides information about the net transmembrane currents that give rise to the measured LFPs. MUA and CSD provide complementary insights into the dynamics of activity within local neural circuits, as MUA primarily reflects suprathreshold neuronal firing (output), while CSD primarily reflects current flow associated with synaptic input, such as excitatory and inhibitory post-synaptic potentials (EPSPs/IPSPs). However, the disentanglement of meaningful functional components of MUA and

CSD derived from trans-laminar LFP signals is an ill-posed problem. MUA contains spikes originating from different populations of excitatory and inhibitory neurons, and CSD is a spatial mixture of extracellular sinks and sources that can be either active (i.e., synaptic activity) or passive (i.e., return currents). Excitatory synaptic activity results in an active sink and a passive source, whereas inhibitory synaptic activity results in an active source and a passive sink. Moreover, the interpretation of activity (especially CSD) at later latencies is more uncertain due to the involvement of long-range cortical inputs (Happel et al., 2010). So far, evoked CSD and MUA have been extensively used to characterize tuning curves (Fishman et al., 2000a, 2000b; Fishman & Steinschneider, 2006, 2009; Steinschneider et al., 1998), differentiate responses to different stimuli (e.g., best-frequency [BF] vs. non-BF and standard vs. deviant) (Fishman & Steinschneider, 2012; Lakatos et al., 2020; O'Connell et al., 2011; Schaefer et al., 2015), and compare local neural population responses in different brain regions (e.g., core vs. belt regions of auditory cortex) (Banno et al., 2022). Statistical analyses in these studies mostly focused on neuronal activity occurring at specific latencies (usually within 50ms) in specific cortical layers (usually layer 4 or 2/3). An alternative approach, called laminar population analysis (LPA), was proposed to decompose the recorded LFP and MUA into firing rates of multiple neural populations and corresponding spatial profiles (Einevoll et al., 2007; Głąbska et al., 2014; Głąbska et al., 2016). However, the extracted components were only mapped to excitatory populations, and the connections between populations were indirectly estimated by a template-fitting analysis. In short, despite the high spatial specificity provided by LFPs and CSD analysis, our understanding of the information flow within neural circuits that give rise to these recorded signals is limited by the underdetermined inverse problem (Tenke & Kayser, 2012).

1.2 Cell type-specific activity in auditory cortex

Calcium imaging and optogenetic techniques make it possible to observe the activity of specific neuron types in auditory cortex. The activity of pyramidal cells is actively shaped by inhibitory interneurons (Liu et al., 2019). The major inhibitory interneuron types have specific characteristics

with regard to morphology, targets, electrophysiology, and plasticity (Studer & Barkat, 2022), and appear to play distinct functional roles in cortical information processing (Blackwell & Geffen, 2017). Parvalbumin-expressing (PV) interneurons are fast-spiking neurons and mostly show higher spontaneous and tone-evoked firing rates than excitatory neurons. They target the soma, proximal dendrites, and initial segment of the axon of excitatory neurons, providing efficient and strong inhibition to excitatory neurons within the cortical column (a radius of up to 130 μm). PV interneurons receive inputs from both local excitatory neurons and the thalamus (MGBv). Functionally, PV interneurons are thought to contribute to the balance of excitation and inhibition and to the control of bottom-up (feedforward) information flow (Hamilton et al., 2013). Somatostatin-expressing (SOM) interneurons, on the other hand, show lower spontaneous and tone-evoked firing rates than PV interneurons. They target the distal dendrites of excitatory neurons, and their inhibition can reach widely (a radius of up to 300 μm) along the tonotopic axis. SOM interneurons receive excitatory inputs mainly within the cortex and much less from the thalamus (Ji et al., 2016). The synapses from excitatory to SOM interneurons are short-term facilitating, whereas the synapses between various types of neurons (e.g, the excitatory synapses between pyramid cells and fast-spiking PV neurons) are mostly short-term depressing (Hayut et al., 2011). SOM interneurons show slower activation dynamics and wider lateral inhibition than PV interneurons, which suggests a functional role of SOM neurons in integrating information over temporal and spectral domains. PV and SOM interneurons mutually inhibit each other. Both PV and SOM interneurons are inhibited by vasoactive-intestinal-peptide-expressing (VIP) interneurons which provide cross-modal modulation of sensory coding (Bigelow et al., 2019). The complex dynamics and functional roles of the various types of interneurons have been further investigated via modeling studies which considered the structural and functional properties of these different interneurons (Hahn et al., 2022; Park & Geffen, 2020).

1.3 Existing biological models

Biological models have been used to bridge the gap between microscopic properties (e.g., neuron types, single-unit neurophysiology, and morphology) and meso-/macroscopic observations (e.g., LFP/EEG/MEG signals). These models vary in their level of detail and scope. For example, a single-column model of the primary visual cortex (consisting of excitatory and inhibitory neurons in layers 2/3, 4, 5, and 6) was constructed to simulate laminar LFPs under different input conditions (Hagen et al., 2016, 2018). A single-column model of the primary auditory cortex (consisting of E, PV, SOM, VIP, and Neurogliaform cells in six layers) was recently constructed to simulate LFP, CSD, and EEG signals that replicate many experimental observations such as spontaneous neural activity and evoked responses to speech input (Dura-Bernal et al., 2022). Such detailed single-column models predict the contribution of layer- and cell-type-specific neuronal populations when the simulations match experimental observations. Some other, less detailed, models have been constructed to account for the generation of evoked responses. A single-column model (consisting of excitatory and inhibitory neurons in layers 2/3 and 5) using Human Neocortical Neurosolver suggests the contribution of a sequence of bottom-up thalamic inputs (targeting the soma of pyramidal neurons and causing upward currents) and top-down cortical inputs (targeting dendrites of pyramidal neurons and causing downward currents) (Kohl et al., 2022; Lakatos et al., 2020). This single-column model relates the ERP/ERF to intracellular currents in pyramidal long dendrites but leaves the origins of the sequences of inputs unexplained. This issue was addressed by a rate-based core-belt-parabelt model that includes an entire network of brain regions comprising auditory cortex (208 cortical columns, each column consisting of one excitatory and one inhibitory population), where ERFs are considered as the weighted sum of spatially distributed damped harmonic oscillators emerging out of coupled excitation and inhibition (Hajizadeh et al., 2019, 2021, 2022). This model provides a holistic perspective on the generation of ERFs. However, the proposed damped modes are extractions from the whole network dynamics, which can be difficult to link with LFP observations for validation. There

remain several principal shortcomings in modeling evoked responses. On the one hand, models that take into account neuronal details (e.g., various types of inhibitory neurons) lack a sufficient consideration of inter-column or inter-area interaction. On the other hand, models that focus on network dynamics and mechanisms provide less information about the role of different inhibitory neurons, and the simulations only qualitatively match the LFP/EEG/MEG recordings. Hence, there is a need for biological models that incorporate both a high degree of detail and a broad scope to clarify the neural underpinnings of cortical evoked responses.

1.4 Goals and approach of this study

In this study, we attempt to overcome the above-mentioned limitations by developing a multi-column model of auditory cortex with sufficient detail regarding neural populations and their interconnections to quantitatively reproduce layer-specific intracranial LFP recordings and qualitatively explain extracranially observable evoked responses. We utilized a biological cortical column model accounting for cell-type-specific interactions, which was integrated into a minimalistic multi-column array, representing the most relevant aspects of cortical architecture with respect to the tonotopic processing of auditory stimuli. Model parameters were specified by fitting the model to LFPs of tone-evoked responses simultaneously recorded across the layers of primary auditory cortex (A1) of awake monkeys. We show that the proposed model not only consistently replicates and explains detailed features of tone-evoked LFPs in A1, but also reproduces relevant aspects of extracranially-recorded evoked responses and predicts cell-type specific contributions to these signals.

2 Methods

2.1 Experimental data

2.1.1 Acquisition and preprocessing

Neurophysiological data were obtained from A1 in 3 adult male macaque monkeys (Macaca fascicularis) using previously described methods (Fishman & Steinschneider, 2010; Steinschneider et al., 2003). All experimental procedures were reviewed and approved by the Association for Assessment and Accreditation of Laboratory Animal Care-accredited Animal Institute of Albert Einstein College of Medicine and were conducted in accordance with institutional and federal guidelines governing the experimental use of non-human primates. Animals were housed in our Association for Assessment and Accreditation of Laboratory Animal Care-accredited Animal Institute under daily supervision of laboratory and veterinary staff. Before surgery, monkeys were acclimated to the recording environment and were trained to perform a simple auditory discrimination task (see below) while sitting in custom-fitted primate chairs.

Surgical procedure. Under pentobarbital anesthesia and using aseptic techniques, rectangular holes were drilled bilaterally into the dorsal skull to accommodate epidurally placed matrices composed of 18-gauge stainless steel tubes glued together in parallel. Tubes served to guide electrodes toward A1 for repeated intracortical recordings. Matrices were stereotaxically positioned to target A1 and were oriented to direct electrode penetrations perpendicular to the superior surface of the superior temporal gyrus, thereby satisfying one of the major technical requirements of one-dimensional current source density (CSD) analysis (Müller-Preuss & Mitzdorf, 1984; Steinschneider et al., 1992). Matrices and Plexiglas bars, used for painless head fixation during the recordings, were embedded in a pedestal of dental acrylic secured to the skull with inverted bone screws. Perioperative and postoperative antibiotic and anti-inflammatory medications were always administered. Recordings began after at least 2 weeks of postoperative recovery.

Stimuli. Stimuli were generated and delivered at a sample rate of 48.8 kHz by a PC-based system using an RX8 module (Tucker Davis Technologies). Frequency response functions (FRFs) derived from responses to pure tones characterized the spectral tuning of the cortical sites. Pure tones used to generate the FRFs ranged from 0.15 to 18.0 kHz, were 200 ms in duration (including 10 ms linear rise/fall ramps), and were randomly presented at 60 dB SPL with a stimulus onset-to-onset interval of 658 ms. Resolution of FRFs was 0.25 octaves or finer across the 0.15–18.0 kHz frequency range tested. All stimuli were presented via a free-field speaker (Microsatellite; Gallo) located 60 degrees off the midline in the field contralateral to the recorded hemisphere and 1 m away from the animal's head (Crist Instruments). Sound intensity was measured with a sound level meter (type 2236; Bruel and Kjaer) positioned at the location of the animal's ears. The frequency response of the speaker was flat (within 5 dB SPL) over the frequency range tested.

Recordings. Neurophysiological recordings were conducted in an electrically shielded, sound-attenuated chamber. Monkeys were monitored via video camera throughout each recording session. To promote alertness and attention to the sounds during the recordings, animals performed a simple auditory discrimination task (detection of a randomly presented noise burst interspersed among test stimuli) to obtain liquid rewards.

Local field potentials (LFPs) and multiunit activity (MUA) were recorded using linear-array multi-contact electrodes, comprising 16 contacts, evenly spaced at 150-micron intervals (U-Probe; Plexon). Individual contacts were maintained at an impedance of 200 kΩ. An epidural stainless-steel screw placed over the occipital cortex served as the reference electrode. Neural signals were bandpass filtered from 3 Hz to 3 kHz (roll-off 48 dB/octave) and digitized at 12.2 kHz using an RA16 PA Medusa 16-channel preamplifier connected via fiber-optic cables to an RX5 data acquisition system (Tucker-Davis Technologies). LFPs time-locked to the onset of the sounds were averaged on-line by computer to yield auditory evoked potentials (AEPs). CSD analyses of the AEPs characterized the laminar

distribution of net current sources and sinks within A1 and were used to identify the laminar location of concurrently recorded AEPs and MUA (Steinschneider et al., 1992, 1994). CSD was calculated using a 3-point algorithm that approximates the second spatial derivative of voltage recorded at each recording contact (Freeman & Nicholson, 1975; Nicholson & Freeman, 1975). MUA used to characterize the frequency tuning of each recording site (i.e., electrode penetration) was derived from the spiking activity of neural ensembles recorded within lower lamina 3, as identified by the presence of a large-amplitude initial current sink that is balanced by concurrent superficial sources in mid-upper lamina 3 (Fishman et al., 2001; Steinschneider et al., 1992). This current dipole configuration is consistent with the synchronous activation of pyramidal neurons with cell bodies and basal dendrites in lower lamina 3. Previous studies have localized the initial sink to the thalamorecipient zone layers of A1 (Metherate & Cruikshank, 1999; Müller-Preuss & Mitzdorf, 1984; Steinschneider et al., 1992; Sukov & Barth, 1998). To derive MUA, neural signals (3 Hz to 3 kHz pass-band) were high-pass filtered at 500 Hz (roll-off 48 dB/octave), full-wave rectified, and then low-pass filtered at 520 Hz (roll-off 48 dB/ octave) before averaging of single-trial responses (for a methodological review, see (Supèr & Roelfsema, 2005)). MUA is a measure of the envelope of summed (synchronized) action potential activity of local neuronal ensembles (Brosch et al., 1997; O'Connell et al., 2011; Schroeder et al., 1998; Supèr & Roelfsema, 2005; Vaughan H.G.Jr, 1988). Thus, whereas firing rate measures are typically based on threshold crossings of neural spikes, MUA, as derived here, is an analog measure of spiking activity in units of response amplitude (e.g., see (Kayser et al., 2007)). MUA and single-unit activity, recorded using electrodes with an impedance similar to that in the present study, display similar orientation and frequency tuning in primary visual and auditory cortex, respectively (Kayser et al., 2007; Supèr & Roelfsema, 2005). Adjacent neurons in A1 (i.e., within the sphere of recording for MUA) display synchronized responses with similar spectral tuning, a fundamental feature of local processing that may promote high-fidelity transmission of stimulus information to subsequent cortical areas (Atencio & Schreiner, 2013).

Positioning of electrodes was guided by online examination of click-evoked AEPs. Pure tone stimuli were delivered when the electrode channels bracketed the inversion of early AEP components and when the largest MUA and initial current sink were situated in middle channels. Evoked responses to 40 presentations of each pure tone stimulus were averaged with an analysis time of 500 ms that included a 100 ms pre-stimulus baseline interval. The BF of each cortical site was defined as the pure tone frequency eliciting the maximal MUA within a time window of 0-75 ms after stimulus onset. This response time window includes the transient “On” response elicited by sound onset and the decay to a plateau of sustained activity in A1 (e.g., see (Fishman & Steinschneider, 2009)).

At the end of the recording period, monkeys were deeply anesthetized with sodium pentobarbital and transcardially perfused with 10% buffered formalin. Tissue was sectioned in the coronal plane (80 m thickness) and stained for Nissl substance to reconstruct the (Morel et al., 1993) electrode tracks and to identify A1 according to previously published physiological and histological criteria (Kaas & Hackett, 2000; Merzenich & Brugge, 1973; Morel et al., 1993). Based upon these criteria, all electrode penetrations considered in this report were localized to A1, although the possibility that some sites situated near the low-frequency border of A1 were located in field R cannot be excluded.

2.1.2 Preparation for model fitting

The target data for model fitting are comprised of the laminar MUA and CSD profiles of evoked responses to the best frequency (BF, see an example in Figure 1) and 4 non-BF tones at four recording sites (site 1 from monkey A, site 2 from monkey D, sites 3 and 4 from monkey E). For each recording site, the experimental data were cropped (time window: 0 to 200 ms, 200 timepoints), concatenated along the time axis, and normalized to their maximum peak, resulting in target MUA [1000 timepoints × 16 channels] and target CSD [1000 timepoints × 12 channels] for model fitting.

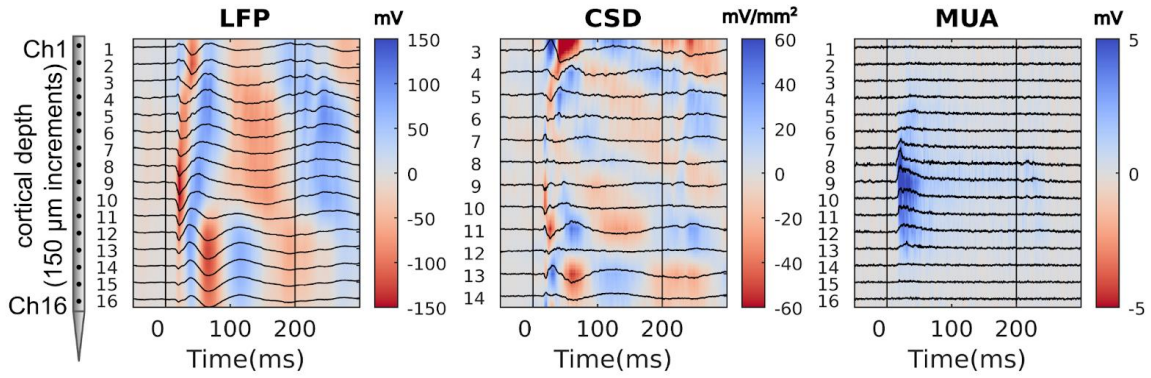

278 *Figure 1. Laminar profiles of evoked responses to a BF tone recorded in a representative electrode*
279 *penetration into A1. The 16-channel electrode array records local field potentials (LFPs) from*
280 *superficial to deep layers (2000 µm), from which current source density (CSD) and multi-unit activity*
281 *(MUA) are derived. A schematic of the electrode array is shown on the left of the figure. For*
282 *visualization, the values of response amplitude are also color-coded (positive values in blue; negative*
283 *values in red). Tone onset and offset times are indicated by the vertical drop lines.*

284

285 ## 2.2 Cortical column model

286 The cortical model consists of two columns. Each column contains 7 neural populations identified by
287 cell type and laminar location of their cell bodies: excitatory pyramidal neurons (L2/3 E, L4 E, and
288 L5/6 E), inhibitory PV interneurons (L2/3/4 PV and L5/6 PV), and inhibitory SOM interneurons (L2/3/4
289 SOM and L5/6 SOM). Each neural population is described by a rate-to-potential operator (Section
290 2.2.4) and a potential-to-rate operator (Section 2.2.5) as in the Jansen-Rit model (Jansen & Rit, 1995).
291 Different types of inhibitory interneurons were considered because of their distinct characteristics
292 regarding morphology, connection motif, target neurons/locations, plasticity, spiking rate, synaptic
293 time constant, and afferent inputs, making it likely that they differentially contribute to the observed
294 MUA and CSD. Thus, the model was designed with the aim of reconstructing the dynamics of different
295 interneuron types from the LFP data. To reduce model complexity, VIP interneurons were not included,

296 as VIP interneurons are thought to be involved in cortico-cortical interaction and neuromodulatory
297 control (Mesik et al., 2015). We would like to note that, within our model framework, the number of
298 neural populations is flexible and its modification would only lead to different degrees of granularity in
299 the spatiotemporal decomposition of MUA and CSD.

300 As illustrated in Figure 2A, column 2 represents a BF recording site (cortical column) that responds
301 optimally to the presented tone stimulus, while column 1 represents an adjacent non-BF recording
302 site that responds sub-optimally to the presented tone stimulus. For simplicity, the configurations of
303 the two columns were set to be identical, and the two columns inhibit each other through symmetric
304 inter-column E-to-SOM connections. The E and PV populations receive direct thalamic input with a
305 fixed ratio based on the literature (see Section 2.2.2). Column 2 (BF site) receives the full strength of
306 thalamic input (in=1), and Column 1 (recording site) receives weaker input (in≤1), based on the
307 tonotopic organization of the auditory pathway. The two-column model is a simplification of the
308 anatomical and functional organization of A1, where the interactions with other cortical areas (e.g.,
309 non-primary fields of auditory cortex) are not considered. In the case of the BF response, both
310 columns receive the same input strength (in=1), as they represent the same location and inter-column
311 connections are in fact intra-column connections. Thus, the same model could be used for both BF
312 and non-BF situations.
313
314 The model simulates the time series of latent variables including firing rates, postsynaptic potentials
315 (PSP), and connectivity efficacy (related to short-term plasticity) under BF and non-BF conditions
316 given the same model parameter settings but different input configurations. As illustrated in Figure
317 2B, the network dynamics are transformed into simulated MUA and CSD via a forward model (see
318 Section 2.3) to match the target data. The forward model also transforms network dynamics to a
319 simulated equivalent current dipole (ECD) signal, which is equivalent (up to a scaling factor

320 determined by the volume conduction of the head) to EEG/MEG signals. Thus, the model could be
321 used to identify the specific contributions of different cell types to those signals.
322

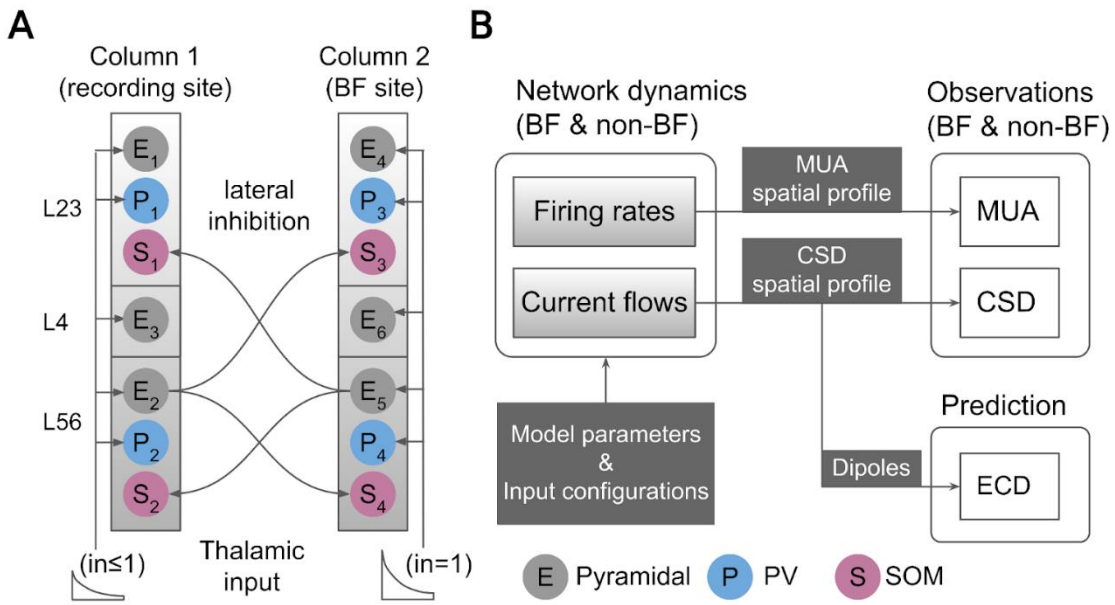

323 *Figure 2. Two-column cortical model and forward simulation. (A) The model consists of two identical*
324 *columns, where Column 1 represents the cortical area at the recording site, and Column 2 represents*
325 *the latent cortical area that responds most strongly to the presented tonal stimulus (at the BF). The*
326 *thalamic inputs make synaptic connections with the E and PV populations at L2/3, L4, and L5/6. The*
327 *lateral inhibition consists of the connections from L5/6 E to the SOM populations at L2/3 and L5/6.*
328 *For clarity, intra-column connections are not shown. (B) The forward simulation includes two stages.*
329 *First, the network dynamics are simulated based on the model parameters and input configurations*
330 *under BF and non-BF conditions at the recording site. Second, the observation model translates firing*
331 *rates and current flows to the observations (i.e., MUA and CSD) through the spatial profiles calculated*
332 *by constrained least square fit. The current flows and CSD can be further translated to dipole signals*
333 *as model predictions.*

2.2.1 Thalamic input

The thalamic input $i_{th}(t)$ to the two-column model is a decay function with a delay (Eq. (1)). The parameters include the decay time constant τ_{in}, decay level α, and delay t_d. This is to mimic the fast decaying firing rate observed in the auditory system (Pérez-González & Malmierca, 2014).

$$i_{th}(t) = \begin{cases} \alpha + (1-\alpha)e^{\frac{t_d - t}{\tau_{in}}}, & t \geq t_d \\ 0, & t < t_d \end{cases} \quad (1)$$

2.2.2 Connectivity

The default intra-column connectivity (Table 1) is derived from the reported connection probabilities and synaptic strengths in the primary visual cortex of mice (Billeh et al., 2020). The inter-column connections only consist of E-to-SOM connections (L5/6 E to L2/3/4 SOM and L5/6 E to L5/6 SOM), with the same ratio as the intra-column E-to-SOM connections.

Table 1A. Connection probabilities after averaging across layers.

To \ From	E1	E2	E3	PV1	PV2	SOM1	SOM2
E1 (L2/3)	0.1600	0.0105	0.1400	0.3305	0.0500	0.3370	0.0845
E2 (L5/6)	0.0415	0.0503	0.0680	0.0395	0.1713	0.0118	0.1192
E3 (L4)	0.0160	0.0035	0.2430	0.2435	0.0500	0.2005	0.0280
PV1 (L2/3/4)	0.2390	0.0250	0.2650	0.2505	0.0340	0.4535	0.0075
PV2 (L5/6)	0.0405	0.0670	0.0505	0.0410	0.1202	0.0075	0.2368
SOM1(L2/3/4)	0.1325	0.0250	0.3355	0.0400	0.0075	0.0660	0.0057
SOM2 (L5/6)	0.0510	0.0508	0.0640	0.0075	0.0425	0	0.0325

Table 1B. Synaptic strengths (unitary PSP [mV]) after averaging across layers.

To \ From	E1	E2	E3	PV1	PV2	SOM1	SOM2
E1 (L2/3)	0.3600	0.2350	0.7800	0.5200	0.4050	0.3050	0.1250
E2 (L5/6)	0.3700	0.5800	0.7950	0.2325	0.8100	0.1250	0.2700
E3 (L4)	0.3400	0.1900	0.8300	0.6000	0.4050	0.2950	0.1400
PV1 (L2/3/4)	1.4400	0.6250	1.3400	0.6800	0.3625	0.5000	0.1125
PV2 (L5/6)	0.6600	2.5000	0.6250	0.4325	1.1900	0.1125	0.4000
SOM1(L2/3/4)	0.7750	0.2600	0.6000	0.4200	0.1050	0.1500	0.1675
SOM2 (L5/6)	0.2650	0.5200	0.2600	0.1050	0.4100	0.0700	0.4000

*Table 1C. Intra-column connectivity (connection probability*synaptic strength).*

To \ From	E1	E2	E3	PV1	PV2	SOM1	SOM2
E1 (L2/3)	0.0576	0.0025	0.1092	0.1719	0.0203	0.1028	0.0106
E2 (L5/6)	0.0154	0.0291	0.0541	0.0092	0.1387	0.0015	0.0322
E3 (L4)	0.0054	0.0007	0.2017	0.1461	0.0203	0.0591	0.0039
PV1 (L2/3/4)	0.3442	0.0156	0.3551	0.1703	0.0123	0.2268	0.0008
PV2 (L5/6)	0.0267	0.1675	0.0316	0.0177	0.1431	0.0008	0.0947
SOM1(L2/3/4)	0.1027	0.0065	0.2013	0.0168	0.0008	0.0099	0.0010
SOM2 (L5/6)	0.0135	0.0264	0.0166	0.0008	0.0174	0	0.0130

The thalamic input is fed only to E and PV populations. The default ratio of input strengths across layers (as listed in Table 2) is based on the peak amplitude of thalamocortical responses and the laminar pattern of thalamocortical innervation in mouse primary auditory cortex reported in (Ji et al., 2016).

Table 2. The ratio of thalamic input strengths across laminar layers (normalized to L4 E).

Neural population	(a) Peak amplitude	(b) % Innervated	(a*b) Relative input strengths
L2/3 E	129/418=0.3	75%	0.225
L4 E	418/418=1	100%	1
L5/6 E	163/418=0.4	85%	0.34
L2/3/4 PV	615/418=1.47	85%	1.25
L5/6 PV	426/418=1.02	100%	1.02

(a) Thalamocortical input currents (pA). Source: Table 1 in (Ji et al., 2016)*.*

(b) Percentage of cells exhibiting thalamocortical responses. Source: Fig. 4 in (Ji et al., 2016)*.*

2.2.3 Rate-to-potential operator

The rate-to-potential operator implements the transformation of the firing rate $r_j(\mathrm{t})$ of the *j*th population to the postsynaptic potential $v_{ij}(\mathrm{t})$ at the *i*th population through an effective connection strength $w_{ij}(\mathrm{t})$. This transformation is achieved by convolving the weighted firing rate $w_{ij}(\mathrm{t})r_j(\mathrm{t})$ with a synaptic kernel $h_{ij}(t)$ (Eq. (2)). Note that the effective connection strength $w_{ij}(t)$ can become a variable, if short-term plasticity is taken into account (see Section 2.2.5).

$$v_{ij}(t) = \left[w_{ij}(t)r_j(t)\right] \otimes h_{ij}(t) \tag{2}$$

The synaptic kernel $h(\mathrm{t})$ is described as a bi-exponential function parameterized by the scaling factor H and the time constants τ_1 and τ_2 (Eq. (3)).

$$h(t) = \begin{cases} H\dfrac{\tau_1\tau_2}{\tau_1-\tau_2}\left(e^{\frac{-t}{\tau_1}} - e^{\frac{-t}{\tau_2}}\right), & t \geq 0 \\ 0, & t < 0 \end{cases} \tag{3}$$

The convolution in Eq. (2) can be numerically realized by two first-order ordinary differential equations (Eqs. (4) and (5)).

$$\dot{v}(t) = u(t) \tag{4}$$

$$\dot{u}(t) = Hw(t)r(t) - \frac{\tau_1 + \tau_2}{\tau_1 \tau_2} u(t) - \frac{1}{\tau_1 \tau_2} v(t) \quad (5)$$

371

372 The shape of synaptic kernels depends on pre- and postsynaptic properties of the neurotransmitter-

373 receptor systems, and the respective parameters H, τ_1, and τ_2 are listed in Table 3.

374

375 *Table 3. Parameters of the synaptic-dendritic kernels for different connections.*

Synaptic type		H	τ_1(ms)	τ_2(ms)	Reference
E→E(1)	AMPA	14400	1	5.3	(Dura-Bernal et al., 2022)
	NMDA	1200	3	70	
E→PV	NMDA	7250	2.1	5.6	(Jouhanneau et al., 2018)
E→SOM	NMDA	3090	4.5	25.2	(Jouhanneau et al., 2018)
PV→E	$GABA_A$	-4000	1	18.2	(Dura-Bernal et al., 2022)
PV→PV	$GABA_A$	-5530	3.5	5.5	(Bacci et al., 2003)
PV→SOM	$GABA_A$	-7380	1.4	101	(Bacci et al., 2003)
SOM→E(2)	$GABA_A$	-1800	2	100	(Dura-Bernal et al., 2022)
	$GABA_B$	-100	25	300	
SOM→PV	$GABA_A$	-1800	2	100	(Dura-Bernal et al., 2022)

376 *(1) AMPA:NMDA=83:17*

377 *(2) $GABA_A$:$GABA_B$=50:50*

378

379 The PSPs $v(t)$ are then used to calculate the current flows $c(t)$. In Eq. (6), a current flow $c_j(t)$

380 caused by the *j*th input source (from a cortical or a thalamic input) is calculated as the sum of the

381 absolute values of PSPs $v_{ij}(t)$ at all E populations ($N_E = 3$) at the recording site (i.e., Column 1).

382 The mapping to MUA and CSD is illustrated in Figure 3**.**

$$c_j(t) = \sum_{i}^{N_E} \left| v_{ij}(t) \right| \tag{6}$$

383

384 ### 2.2.4 Potential-to-rate operator

385 The potential-to-rate operator transforms the overall PSP $v_i(\mathrm{t})$ at the *i*th population into mean firing
386 rate $r_i(t)$ using a sigmoid function (Eqs. (7) and (8)). The overall PSP is the sum of EPSPs and
387 IPSPs caused by N_{cur} presynaptic current sources which include N_{pop} excitatory/inhibitory
388 populations and thalamic input.

389

$$r_i(t) = Sigm[v_i(t)] = Sigm\left[\sum_{j}^{N_{cur}} v_{ij}(t)\right] \tag{7}$$

$$Sigm(v) = \begin{cases} \dfrac{1}{1+e^{r(v_0-v)}} - \dfrac{1}{1+e^{rv_0}}, & v \geq 0 \\ 0, & v < 0 \end{cases} \tag{8}$$

390

391 The output firing rate is limited to $0 \leq r(t) \leq 1$, where $r = 1$ refers to the max firing rate of the
392 E/PV/SOM neuron type. The sigmoid function is shifted so that $Sigm(0) = 0$, meaning no change in
393 the firing rate relative to baseline. To make the fitting process more stable, negative firing rates are
394 set to 0. The sigmoid functions for the E, PV, and SOM populations have different slopes r and
395 thresholds v_0 (as listed in Table 4) based on the firing characteristics of the neuron types reported
396 in (Fanselow et al., 2008).

397

398 *Table 4. Parameters of the sigmoid functions*

	r (mV^{-1})	v_0 (mV)
E	0.62	6

PV	0.29	15.6
SOM	1.14	2.76

2.2.5 Short-term plasticity

Short-term plasticity (STP) refers to the modulation of synaptic strength based on the history of presynaptic activity. STP can be depressing (STD) or facilitating (STF), which depends on the synaptic type (Blackman et al., 2013; Fino et al., 2013; Ma et al., 2012; Regehr, 2012; Silberberg et al., 2005). STD can be modeled by a synaptic efficacy variable x $(0 \leq x \leq 1)$, which denotes the fraction of remaining neurotransmitters (or synaptic vesicles). STF can be modeled by another synaptic utilization variable u $(0 \leq u \leq 1)$ which denotes the neurotransmitters ready for use (release probability) (Silberberg & Markram, 2007). The two variables then modulate the fixed connection strength w_0 as in Eq. (9).

$$w(t) = x(t)u(t)w_0 \tag{9}$$

The variables $u(t)$ and $x(t)$ depend on the presynaptic firing rate $r(t)$ as in Eqs. (10) and (11). The parameter U is the initial release probability, and parameters τ_f and τ_d denote the decay and recovery time constants, respectively. The parameters κ_f and κ_d are the change rates and are tuned in the optimization procedure.

$$\dot{u}(t) = \frac{U - u(t)}{\tau_f} - \kappa_f U[1 - u(t)]r(t) \tag{10}$$

$$\dot{x}(t) = \frac{1 - x(t)}{\tau_d} - \kappa_d u(t)x(t)r(t) \tag{11}$$

The effect of STP on the dynamics of a network of E, PV, and SOM populations has been studied by Hayut and colleagues (Hayut et al., 2011). Among the eight synaptic types, only E-to-SOM connections exhibit STF, while the remaining connections exhibit STD. To simplify the model, we consider STF on E-to-SOM connections and STD on E-to-E connections in the model. This decision is based on two considerations. First, the SOM activity is relatively slow compared with E and PV, so its functionality with STF is a focus in our study. Second, Both E and PV display faster responses than SOM. The effect of STD on E-to-PV, PV-to-E, and PV-to-PV connections may cancel each other, and therefore, the gross effect could be integrated into STD on E-to-E connections. The parameters of STP are based on (Hayut et al., 2011; Silberberg & Markram, 2007). See Table 5 for details.

Table 5. Parameters of short-term plasticity.

	U	τ_f (ms)	τ_d (ms)	κ_f	κ_d
E→E	1	-	200	0	20*
E→SOM	0.05	670	-	600*	0

*Note: Values marked by * are default values that will be rescaled by free parameters.*

2.3 Observation model

The observation model includes two spatial profiles which map the network dynamics to MUA and CSD. To match the target data, the network dynamics are subsampled to $T = 200$ timepoints (i.e., firing rates r into S_{rate} $[N_{pop} \times T]$, and current flows c into $S_{current}$ $[N_{cur} \times T]$, where $N_{pop} = 7$ populations, and $N_{cur} = 8$ input sources.

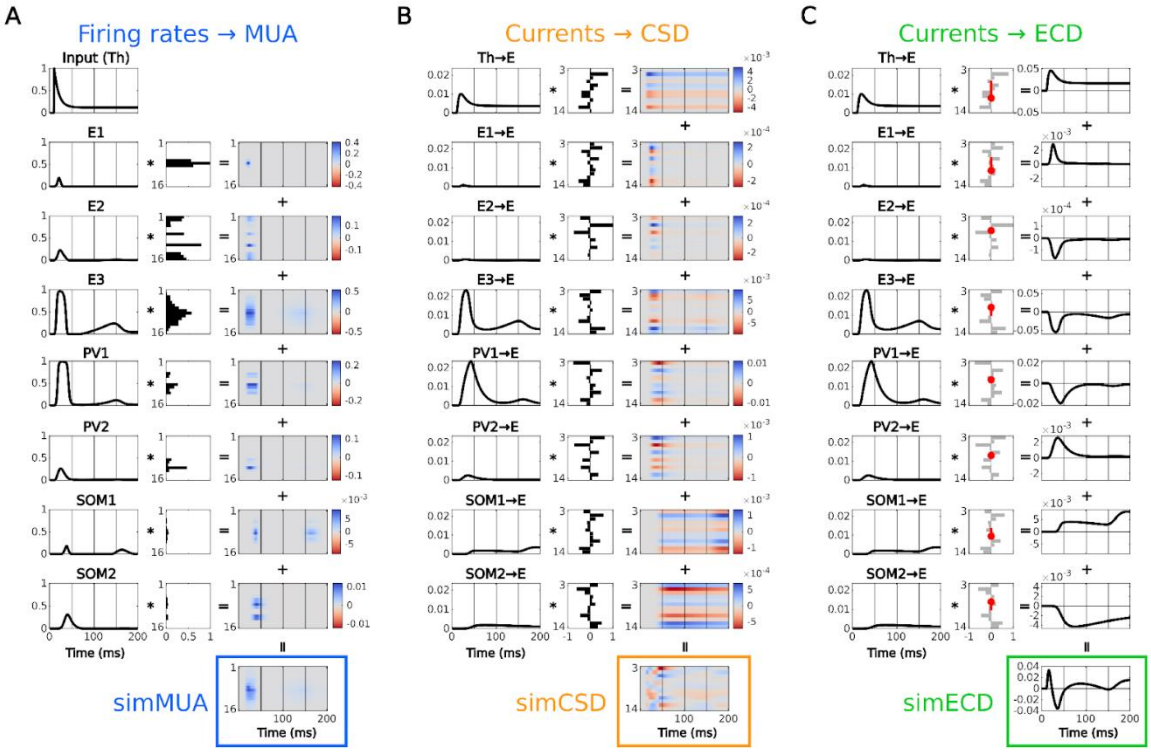

Figure 3. Forward mapping from network dynamics to observations. (A) The simulated MUA (simMUA) is the sum of individual firing rates (left column) weighted by the non-negative MUA spatial profile (middle column) of the recording site (Column 1). (B) The simulated CSD (simCSD) is the sum of individual current flows (left column) weighted by the CSD spatial profile (middle column) of the recording site (Column 1). (C) The simulated equivalent current dipole (simECD) is the sum of individual current flows (left column) weighted by dipole directions and lengths (red lines in the middle column, red dots: centers of current sinks) derived from the CSD spatial profile (gray color in the middle column).

2.3.1 Spatial profiles

The MUA spatial profile A_{MUA} [N_{ch}×N_{pop}] describes the sensitivity of channels ($N_{ch} = 16$) to the firing rates of neural populations, which is closely related to the spatial distribution of cell bodies (or axonal hillocks, where the spikes are generated). The simulated MUA Φ_{MUA} [N_{ch}×T] is the multiplication of the mixing matrix A_{MUA} and the firing rates S_{rate} (Eq. (12)).

$$\Phi_{MUA} = A_{MUA} \cdot S_{rate} \quad (12)$$

The CSD spatial profile A_{CSD} [$N_{ch'} \times N_{cur}$] describes the sensitivity of the spatial distribution of sinks and sources along the channels ($N_{ch'} = 12$) to the current flows. The simulated CSD Φ_{CSD} [$N_{ch'} \times T$] is the multiplication of the mixing matrix A_{CSD} and the current flows $S_{current}$ (Eq. (13)).

$$\Phi_{CSD} = A_{CSD} \cdot S_{current} \quad (13)$$

2.3.2 Constraints on the spatial profiles

Both spatial profiles A_{MUA} and A_{CSD} are difficult to determine by measurements. They are estimated by constrained regression of the network dynamics S_{rate} and $S_{current}$ to the target data Φ_{MUA}^{ref} and Φ_{CSD}^{ref}. The goal is to find spatial profiles that minimize the distance between simulation Φ and target Φ^{ref}, while, at the same time, obeying certain plausibility constraints.

The constraint on the MUA spatial profile A_{MUA} [$N_{ch} \times N_{pop}$] is based on the fact that the sensitivity to the firing rate of a certain cell type is proportional to the product of cell density and maximum firing rate. Therefore, the ratios of the column sums of A_{MUA} should be fixed. The cell densities (E: 128400, PV: 4345, SOM: 2142 cells/mm^3) are estimated from (Keller et al., 2018), and the maximum firing rates (E: 59.4 Hz, PV: 271.7 Hz, SOM: 120.7 Hz) are based on (Beierlein et al., 2003).

The constraint on the CSD spatial profile A_{CSD} [$N_{ch'} \times N_{cur}$] is based on the fact that the transmembrane currents should be conserved. Therefore, each column of A_{CSD} should add up to

zero (i.e., area of sinks = area of sources). Additionally, in order to avoid ambiguity with the overall current magnitudes, the norms of all column vectors of A_{CSD} are constrained to be the same.

2.3.3 Equivalent current dipole

The neuronal generators of EEG/MEG signals are commonly estimated as equivalent current dipoles (ECDs) by source localization techniques such as dipole fitting and beamforming. The simulated ECDs provide a theoretical link between LFPs and EEG/MEG signals, by which we can also examine the contribution of E, PV, and SOM populations to event-related deflections, like P1, N1, and N2.

The model predicts Φ_{ECD} [1×T] at the recording site once current flows $S_{current}$ and a CSD spatial profile A_{CSD} are given. As in Eq. (14), Φ_{ECD} is calculated as the multiplication of $\bar{d}$ [1×N_{cur}] and the current flows $S_{current}$ [N_{cur}×T], where $\bar{d}$ is the displacement from the mean center of sinks $\bar{d}_{sink}$ to the mean center of sources $\bar{d}_{source}$ derived from each column of A_{CSD} [$N_{ch'}$×N_{cur}].

$$\Phi_{ECD} = \bar{d} \cdot S_{current} = \left(\bar{d}_{source} - \bar{d}_{sink}\right) \cdot S_{current} \quad (14)$$

2.4 Optimization procedure

In general, we use a genetic searching scheme combined with a gradient descent (Gauss-Newton) method to optimize the 28 free parameters in θ within a predefined search range, in order to minimize the cost function $f(\theta)$ for each recording site. Since the cost function has a complicated shape with multiple local minima, we made use of the assumption that the true solutions should yield similar parameters across recording sites. In order to reliably find these solutions, we iteratively continued the search for each recording site starting at the solutions for all other recording sites. If our assumption is correct, this should lead to better fits for the individual recording sites.

Note that this additional similarity criterion is only used to guide the search for the solutions, while the sole criteria for the goodness of fit are the cost functions for the individual recording sites. The optimization scheme is detailed in Figure 4.

The cost function $f(\theta)$ is defined as the sum of squared errors (SSE) between the simulation $\Phi(\theta)$ and target Φ^{ref} (Eq. (15)). The target data Φ^{ref} comprises Φ^{ref}_{MUA} and Φ^{ref}_{CSD} under BF and non-BF conditions. The benefit of including non-BF conditions in the optimization procedure is two-fold. First, the amount of target data is increased while the degrees of freedom of spatial profiles remain the same, which reduces the risk of overfitting. Second, the dynamics of PV and SOM populations under BF vs. non-BF conditions can be compared.

$$f(\theta) = \left\| \Phi(\theta) - \Phi^{ref} \right\|_2^2 = \sum_i \sum_j \left(\phi_{ij}(\theta) - \phi_{ij}^{ref} \right)^2 \quad (15)$$

The simulated data $\Phi(\theta)$ of an individual recording site comprises of $\Phi_{MUA}(\theta)$ and $\Phi_{CSD}(\theta)$ as in Eqs. (12) and (13). The forward simulation includes two stages. In the first stage, the default two-column model and input configuration are rescaled by 28 free parameters θ to generate network dynamics S_{rate} and $S_{current}$. The 28 free parameters rescale intra-column connections (8 parameters: W_{EE}, W_{PE}, W_{SE}, W_{EP}, W_{PP}, W_{SP}, W_{ES}, and W_{PS}), the ratio of thalamic inputs (2 parameters: $i_{th,E}$ and $i_{th,PV}$), rates of short-term plasticity (2 parameters: $\kappa_{d,EE}$ and $\kappa_{f,SE}$), synaptic time constants (1 parameter: τ), slopes of sigmoid functions (1 parameter: r), thalamic input strengths for non-BF conditions (4 parameters), thalamic input decay levels for BF and non-BF conditions (5 parameters: α), and inter-column E-to-SOM connections for BF and non-BF conditions (5 parameters). The search ranges of the 28 free parameters are listed in Table 6. In the second stage, the spatial profiles A_{MUA} and A_{CSD} are optimized by regressing the resulting network

dynamics S_{rate} and $S_{current}$ to the target Φ_{MUA}^{ref} and Φ_{CSD}^{ref}, respectively. Multiplication of spatial profiles with network dynamics then yields the predicted MUA and CSD, which can be compared to the observed MUA and CSD.

We use the Gauss-Newton (gn) method to approach the minimum of the cost function $f(\theta)$ in Eq. (15). This method was successfully used in our previous studies for optimization of neural mass models with large numbers of free parameters (Wang et al., 2019; Wang & Knösche, 2013). The Jacobian matrix $J = \frac{\partial f}{\partial \theta}$ is numerically approximated with Newton's difference quotient.

The genetic search scheme (see Figure 4) includes three operating boxes for broadening the exploration in parameter space. In the 'mutation' box, the solutions are sorted based on the goodness-of-fit (cost). Then, each parameter of a solution can mutate (i.e., be replaced by a random value) with a chance that linearly ranges from 10% (for best fit case) to 90% (for worst fit case) based on the ranking of the solution.

In the 'cross-over' box, we randomly draw two solutions as parent solutions from the outputs of 'selection' and 'mutation' boxes. Then we randomly decide a cross-over point and generate two off-spring solutions by swapping the same sides of parameters between the parents (i.e. segment-wise swap). This is repeated to generate N_3 solutions.

In the 'mt_co' box, we run the cross-over operator again. However, instead of swapping the whole right side of the cross-over point, we only swap the cross-over point (i.e., element-wise swap). This is repeated to generate N_3 solutions. The parent solutions come from the output of 'selection', 'mutation', and 'cross-over' boxes.

The effect of model parameters on the network dynamics can be highly nonlinear, and a global minimum in cost function is hard to identify in high-dimensional space. In addition, a global minimum for a single recording site may still be at risk of overfitting. Therefore, it is important to check the similarity and stability of the common solutions. We explore the cost function surface by deviating each parameter at a time, starting from a final solution in the parameter space.

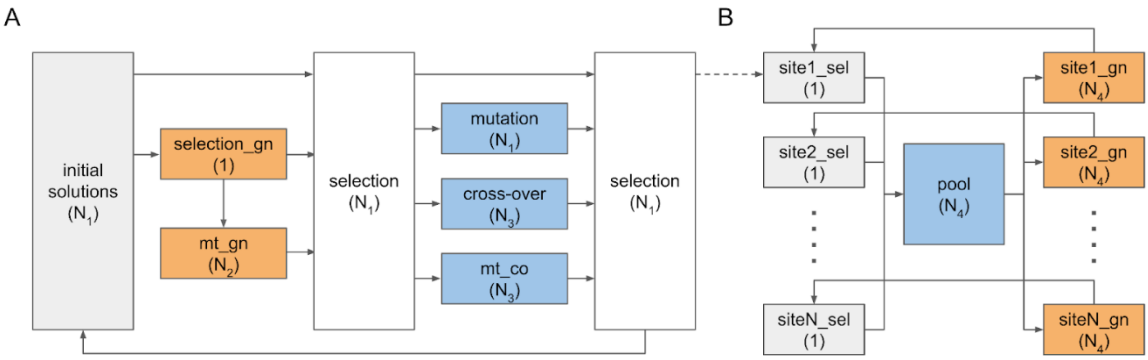

Figure 4. Flow chart of optimization procedure. (A) Optimization for an individual recording site. The iteration starts with $N_1 = 60$ *initial random solutions (parameter sets). The orange box 'selection_gn' selects the best solution (with highest* R^2*) and fine-tunes that solution using the Gauss-Newton (gn) method to the next local minimum. The orange box 'mt_gn' mutates that locally optimal solution, one parameter at a time, resulting in* $N_2 = 28$ *modified solutions. These are then fine-tuned again using the gn method. The white box 'selection' keeps the first* N_1 *solutions with highest* R^2 *from the* $N_1 + 1 + N_2$ *solutions. The blue box 'mutation' creates another* N_1 *solutions, while 'cross-over' and 'mt_co (mutated_cross-over)' boxes each generate* N_3 *random solutions (*$N_3 = 2000$*). The next white box 'selection' again keeps the first (best)* N_1 *solutions from these* $2N_1 + 2N_3$ *solutions and replaces the initial solutions. The best solution for an individual site is selected after 10 iterations. (B) Optimization across recording sites. The iteration starts with the best solution for each recording site. Noise is added to these solutions with a uniform distribution (range:* $\pm std(i), i \in 1,2,\dots,28$*) to generate* $N_4 = 1000$ *jittered solutions in the blue box 'pool'. Each of these jittered solutions is then fine-tuned for*

each recording site with respect to R^2 using the gn method (the orange boxes). The optimized solution for each recording site is updated iteratively if a fine-tuned solution with higher R^2 is found. The iteration ends when there is no update. Then, for each recording site, the best-fitting solution is selected as the final solution. The number in the parentheses in each box indicates the resulting number of solutions.

Table 6. Search ranges of the free parameters.

Free parameters	Default configurations to be rescaled	Range [min, max]
θ_{1-8}	connection strengths W_{EE}, W_{PE}, W_{SE}, W_{EP}, W_{PP}, W_{SP}, W_{ES}, and W_{PS}	[0.1, 10]
$\theta_{9,10}$	Ratio of thalamic inputs $i_{th,E}$ and $i_{th,PV}$	[0.1, 10]
$\theta_{11,12}$	Short-term plasticity $\kappa_{d,EE}$ and $\kappa_{f,SE}$	[0.8, 1.5]
θ_{13}	Synaptic kernel time constants τ	[1, 1]
θ_{14}	Sigmoid function slopes r	[1, 1]
θ_{15-19}	Thalamic input decay levels α (BF and non-BF conditions)	[0.1, 0.3]
θ_{20-24}	Inter-column W_{SE} for lateral inhibition (BF and non-BF conditions)	[1, 15]
θ_{25-28}	Thalamic input strengths to Column 1 (non-BF conditions)	[0.1, 1.2]

2.5 Non-negative matrix factorization

We examined whether a blind decomposition approach would yield similar predictions (e.g., ECD) as our model-fitting approach. The non-negative matrix factorization (a Matlab function *nnmf*) was used to decompose target MUA Φ_{MUA}^{ref} [N_{ch}×T] into two non-negative matrices A_{MUA}^{nnmf} [N_{ch}×N_{pop}] and S_{rate}^{nnmf} [N_{pop} × T] where the root mean square residual between Φ_{MUA}^{ref} and $A_{MUA}^{nnmf} \cdot S_{rate}^{nnmf}$ is

minimized. The decomposed firing rates S_{rate}^{nnmf} are then convolved with alpha kernels to generate current flows $S_{current}^{nnmf}$. The time constants of the alpha kernels are optimized in similar procedure as in Figure 4A to minimize the SSE between Φ_{CSD}^{ref} and $A_{CSD}^{nnmf} \cdot S_{current}^{nnmf}$. The ECD Φ_{ECD}^{nnmf} is then calculated in the same way as in Sections 2.3.3.

3 Results

We fitted the 28 parameters (see Methods section) of our cortical column model, such that the MUA and CSD derived from the electrophysiological data obtained at each recording site were explained best in a least squares sense. Concurrently with the parameters of the cortical column model, we also fitted a set of parameters of the observation model, namely the spatial sensitivity distribution of each neural population (i.e., MUA spatial profile A_{MUA}) and the spatial distribution of current sinks and sources on pyramidal dendrites (i.e., CSD spatial profile A_{CSD}). As a result, the fitted model predicted not only the MUA and CSD that we could compare to the empirically measured values, but also a set of latent (hidden) variables, namely the mean firing rates and the current flows of the neural populations.

In Section 3.1, we present the predicted data (Φ_{MUA} and Φ_{CSD}) along with the target data (Φ_{MUA}^{ref} and Φ_{CSD}^{ref}) for a qualitative and quantitative comparison. In Section 3.2, we show the estimated latent variables, covering neural population activity (firing rates and current flows), as well as the ECD magnitude at the recording sites (ECD, Φ_{ECD}). We also compare Φ_{ECD} with the ECD estimated by a non-negative decomposition approach Φ_{ECD}^{nnmf} to evaluate the advantages of our model-fitting approach. Section 3.3 reports the estimated parameters of the observation model: MUA spatial profile A_{MUA} and CSD spatial profile A_{CSD}. In Section 3.4, we finally examine the fitted parameters of the

595 cortical column model and assess their similarity across the four recording sites (electrode
596 penetrations).
597

598 ## 3.1 Explanation of the target data

599 The waveforms for measured and predicted MUA and CSD for all 4 recording sites are shown in
600 Figure 5. These recording sites were selected to cover a wide range in tonotopic space in A1. More
601 detailed depictions, alongside the goodness of fit (R^2), are given in Figure S1. The target data for
602 model fitting includes the Φ_{MUA}^{ref} and Φ_{CSD}^{ref} of the evoked response to the best frequency (BF) and
603 non-BF tones (see Figure 5 A and B). The BFs of the four recording sites were determined to be 300
604 Hz, 1000 Hz, 500 Hz, and 6400 Hz, respectively. In Φ_{MUA}^{ref}, L4 (centering around Ch 10) shows higher
605 MUA in BF conditions than in non-BF conditions. This corresponds to the frequency selectivity (tuning
606 curves) of neural population responses that give rise to the tonotopic organization of A1. The BF
607 response may include sustained activity (e.g., 500 Hz at site 3) or a second peak after 150 ms (e.g.,
608 300 Hz at site 1). The non-BF responses at recording site 1 (i.e., 200, 260, 400, and 600 Hz) show
609 negative firing rates (after subtraction of the baseline), reflecting the strong effect of lateral inhibition.
610 In Φ_{CSD}^{ref}, there are early L4 sinks and sources (especially clearly seen at sites 2 and 4) followed by
611 sinks and sources at L2/3 and L5/6. There are also slow sinks and sources occurring after 100 ms
612 (especially clearly seen at sites 3 and 4).
613

614 The predicted data Φ_{MUA} and Φ_{CSD} capture the general pattern of target data (Figure 5 C and D).
615 The negative firing rate (relative to the pre-stimulus baseline, as at site 1) cannot be reproduced
616 because we only allow non-negative firing rates and a non-negative MUA spatial profile to avoid
617 overfitting (see Discussion). There are some other minor differences between the simulated and target
618 responses. For example, the sustained firing rate (e.g., 500 Hz at site 3) is not well captured by the
619 model. The patterns in Φ_{MUA} and Φ_{CSD} tend to be sharper and do not capture the smooth

propagation across layers in Φ_{MUA}^{ref}, and Φ_{CSD}^{ref}, which is due to the limited number of populations ($N_{pop} = 7$) in the model.

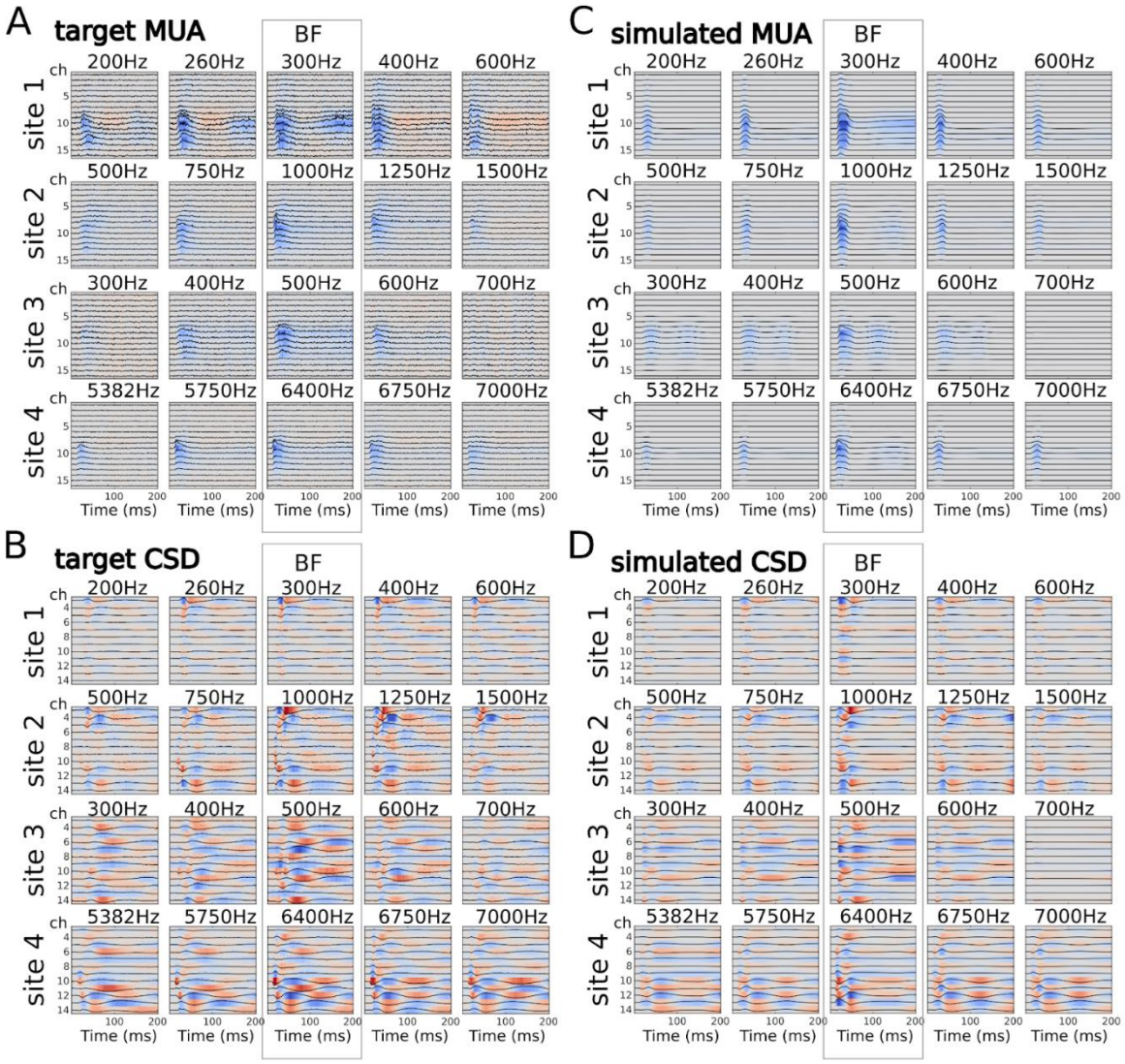

Figure 5. Visual comparison of target data and model simulations. (A, B) Target MUA (A) and CSD (B) at the four recording sites. The rows show the responses to different tone frequencies at each recording site. For example, the 1st row shows responses to 200, 260, 300, 400, and 600 Hz at site 1. The middle column represents the responses to tones at the BF of each recording site (300, 1000, 500, and 6400 Hz, respectively). The other columns represent non-BF responses. In the target data, the maximum value of each row was normalized to 1. (C, D) The simulated MUA (C) and CSD (D)

from the final model solutions. Response amplitudes are color-coded (blue: positive; red: negative).

3.2 Estimated latent variables

3.2.1 Neural activity

The final model solutions provide estimated network dynamics that may underlie the empirical observations. Figure 6 shows the firing rates S_{rate} of Column 1 (representing the recording site) as well as the strength of thalamic inputs based on the common solutions. The network dynamics across the four recording sites share similar patterns. The thalamic inputs are stronger under the BF than the non-BF conditions, which agrees with the tonotopic organization of A1. The direct input connections lead to stronger early peaks in E and PV activity under the BF than the non-BF conditions (early intra-column E→PV effect). In contrast, the early peaks in SOM activity are weaker under the BF than the non-BF conditions. This is due to the excitatory input from Column 2 via E→SOM connections (lateral inhibition, late inter-column E→SOM effect). Additionally, the SOM activity rises higher and lasts longer with short-term facilitation. The BF and non-BF responses show opposite dynamics. The strong PV inhibits SOM in BF responses, whereas the strong SOM inhibits PV in non-BF responses.

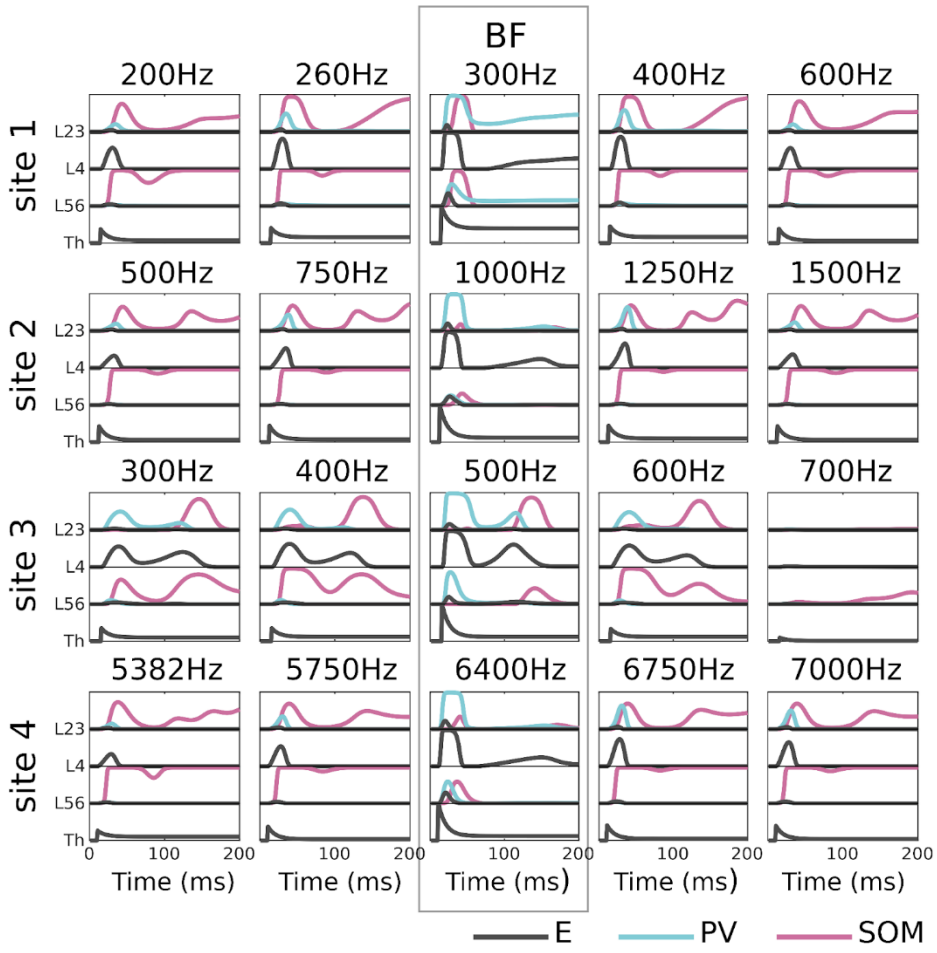

644 *Figure 6. Estimated firing rates under BF and non-BF conditions. The firing rates are grouped into*
645 *layers for visualization (L23: E1, PV1, and SOM1; L4: E3; L56: E2, PV2, and SOM2; Th: thalamic*
646 *input). Note that the layer labeling refers to the original model construction (Figure 2), while the actual*
647 *spatial profiles of the cell bodies arising from the fitting (Figure 8A) deviate from those initial*
648 *assumptions. The PV populations (blue curves) show stronger activity in BF responses (middle*
649 *column) than in non-BF responses, where the peak values are mainly affected by the strength of*
650 *thalamic input (i.e., tonotopy). In contrast, the SOM populations (red curves) show strong and long-*
651 *lasting activity in non-BF responses, which reflects the effect of inter-column E→SOM connections*
652 *(i.e., lateral inhibition).*

3.2.2 Contribution to EEG/MEG components P1, N1, and P2

The equivalent current dipole (ECD) Φ_{ECD} derived at each recording site provides a link between intracranially-recorded LFPs and extracranially-recorded EEG/MEG signals. The ECD can be calculated by Eq. (14), where the current flows associated with activity of specific neural populations contribute to the ECD by different weights and directions based on the CSD spatial profile A_{CSD}. Figure 7A shows the predicted ECDs and the contributions of current flows by the E, PV, and SOM populations at the four recording sites under BF and non-BF conditions. Although there is no ground truth for verification, the predicted ECDs (the black curves in Figure 7A) show deflections that can be related to the EEG/MEG components P1, N1, and P2. The deflections are the net result of the summation and cancellation of current flows. To gain insight into cell-type specific contributions to these deflections, we summed the dipole magnitudes from each of the cell types (while keeping the thalamic input separate), resulting in only four dipole magnitudes (i.e., $\bar{d}_i \cdot S_{current,i}$ where $i \in \{E, PV, SOM, Th\}$ as in Eq. (14)). For example, the PV dipole signals (yellow curves in Figure 7A) represent the gross current flow in pyramidal dendrites (i.e., the IPSP on E1, E2, and E3 populations) elicited by the PV neurons (i.e., PV1 and PV2 populations).

In Figure 7A, we find that the first positive peak of the ECD (related to P1) is consistently due to the thalamic input (purple curves). The first negative peak of the ECD (related to N1) can be due to either the E current (blue curves, sites 2, 3, and 4) or the PV current (red curves, site 1), which depends on the dipole direction derived from the CSD spatial profile. The second positive peak of the ECD (related to P2) can be due to either the decrease in E or PV currents (e.g., blue or red curves, sites 1,2,3, and 4, BF condition) or the increase in SOM current (e.g., yellow curves, sites 2 and 4, non-BF conditions). Based on these predicted ECDs and cell-type specific contributions, the P1 component is likely to result from the thalamic input (including the BF and non-BF columns). The N1 component is likely to result from the activity of E/PV neurons (also including the BF and non-BF columns). The P2

678 component is likely to result from SOM activity (within non-BF columns) and from the decreased
679 activity of E/PV neurons (within BF columns).
680
681 The model fitting approach provides a way to decompose the LFP into temporal and spatial
682 components and predict the ECD at the recording site. We were curious whether a blind
683 decomposition approach would yield similar predictions. To examine this possibility, we decomposed
684 the MUA using non-negative matrix factorization (NNMF), determined optimized current flows and
685 CSD spatial profile, and calculated the dipole signal (Section 2.5). We found that the NNMF approach
686 does not yield reasonable ECDs (Figure 7B) even though the decomposition leads to improved
687 goodness of fit (Figure S2) compared with the model fitting approach. These findings suggest that the
688 model fitting approach can successfully account for the MUA and CSD data and relate them to
689 EEG/MEG signals.

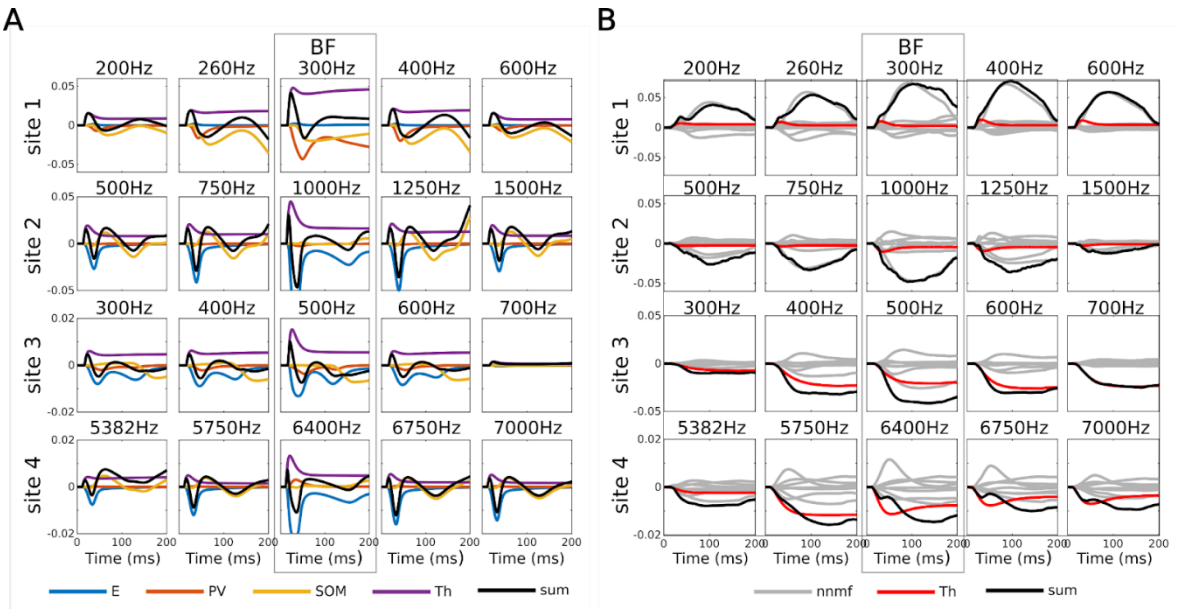

690
691 *Figure 7. Simulated equivalent current dipole (ECD) signals. (A) The simulated ECD (black curves)*
692 *reflects the contribution of a recording site to the EEG/MEG signal (before considering the orientation*
693 *with respect to the MEG sensors). The simulated ECD signal is calculated as the sum of population-*
694 *level CD signals (colored curves) representing the effective current flows along the long dendrites of*

pyramidal cells induced by individual neural populations or thalamic input (E: E1, E2, and E3; PV: PV1 and PV2; SOM: SOM1 and SOM2; Th: thalamic input). (B) Simulated ECD signals obtained by the NNMF approach.

3.2.3 Parameters of the observation model

The observation model contains an MUA spatial profile A_{MUA} and a CSD spatial profile A_{CSD} that project firing rates S_{rate} and current flows $S_{current}$ to observations Φ_{MUA} and Φ_{CSD}. We now check the estimated spatial profiles $\mathrm{A_{MUA}}$ and A_{CSD} provided by the final solutions. The MUA spatial profiles A_{MUA} represent the sensitivity of the 16 laminar electrode channels to the firing rates of neural populations. Figure 8A shows the MUA spatial profile at each recording site (electrode penetration). The distributions of E3 center around channel 10, which is consistent with the distribution of L4 excitatory neurons. However, the distributions of E1 and E2 form one to two clusters, a scenario which does not agree with the expected distribution of excitatory neurons in L2/3 and L5/6. This suggests that the definition of neural populations, after model fitting, do not strictly adhere to the initial laminar definition (i.e., the default connectivity) but changes based on the temporal dynamics of neural activity. This alteration in distribution also applies to the PV and SOM populations. In other words, the estimated connectivity of the column model and the estimated spatial profiles of the observation model should not be directly mapped to the L2/3, L4, and L5/6 categorization.

Figure 8B shows the CSD spatial profile of each recording site, which represents the overall distribution of current sinks and sources along the dendrites of the excitatory cells (incl. E1, E2, and E3). We found that the distributions of sinks and sources interlace and spread widely, and differ across recording sites. This may correspond to the relatively high variability in CSD across recording sites. This may be also due to the fact that the depth of the 16-channel electrode within the cortex is not necessarily identical across the 4 electrode penetrations.

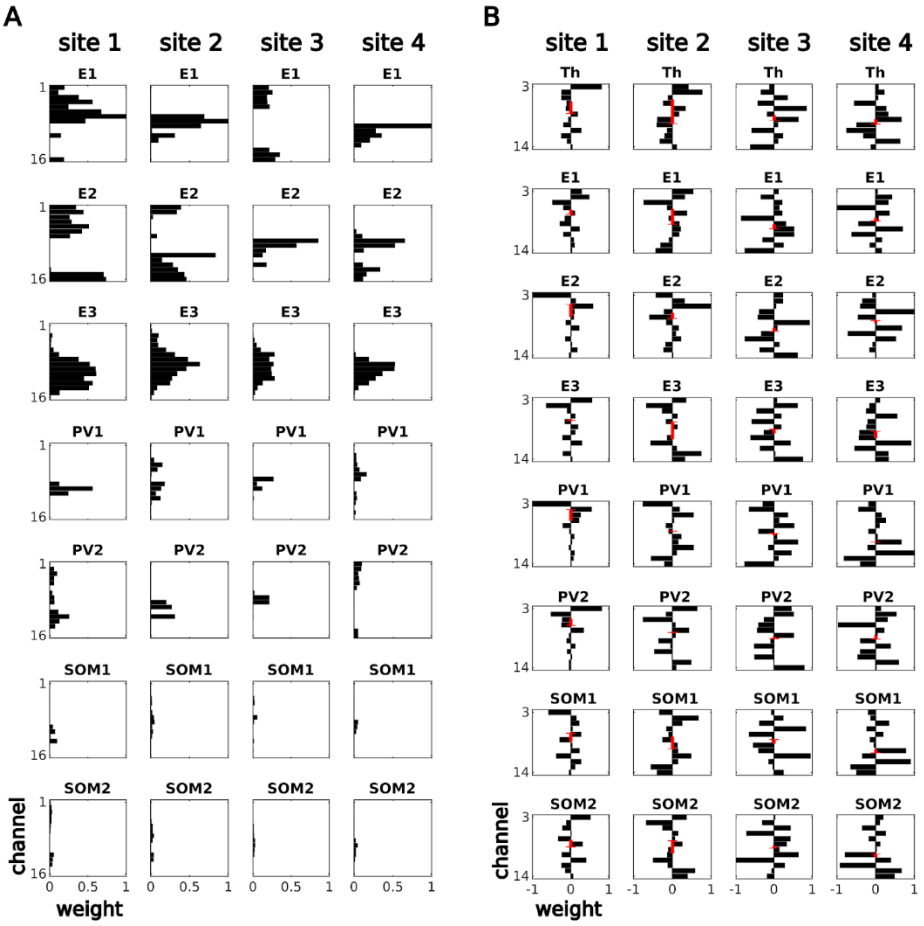

720 *Figure 8. Estimated spatial profiles. (A) MUA spatial profiles. Each column represents the laminar*
721 *distribution (across electrode channels) of firing rates of neural populations within each recording site.*
722 *(B) CSD spatial profiles. Each column represents the corresponding laminar distribution of sinks and*
723 *sources. The red arrow ⊢ indicates the dipole length and direction (from center of sinks to center of*
724 *sources)*

725

726 ## 3.3 Fitted parameters

727 Next, we checked whether the common solutions for the four recording sites share similar patterns.
728 In Figure 9, we show parameters related to the tuning curve and lateral inhibition. The tuning curve is
729 characterized by four parameters (θ_{25-28}) which define the strength of thalamic input to the recording
730 site (Column 1) under the four non-BF conditions. The tone frequencies in Figure 9 are plotted on a

log scale. The input strengths under the four non-BF conditions are all weaker than 0.5, and decrease as the tone frequency becomes more distant from the BF of the neurons, which is consistent with features of spectral tuning curves in A1. The lateral inhibition is characterized by five parameters (θ_{20-24}) which rescale the default strengths of inter-column E-to-SOM connections. We found M-shape lateral inhibition curves, where lateral inhibition increases as the tone frequency deviates from the BF tone but decreases as the tone frequency deviates further. The tuning curves and lateral inhibition curves directly affect the activities of PV and SOM populations, respectively, as demonstrated by the firing rates under BF and non-BF conditions in Figure 9.

We then checked the cost function surface by separately scanning each parameter around the solutions (scanning ranges as listed in Table 6). The surfaces of the four recording sites are shown in Figure 10. In general, we found that the values of solutions (indicated by triangles) are close to each other in the scan range, and the cost (normalized SSE) increases as the values deviate from the solutions. This satisfies our expectations that the four final solutions are close in the parameter space, and that at least local minima of the cost function exist.

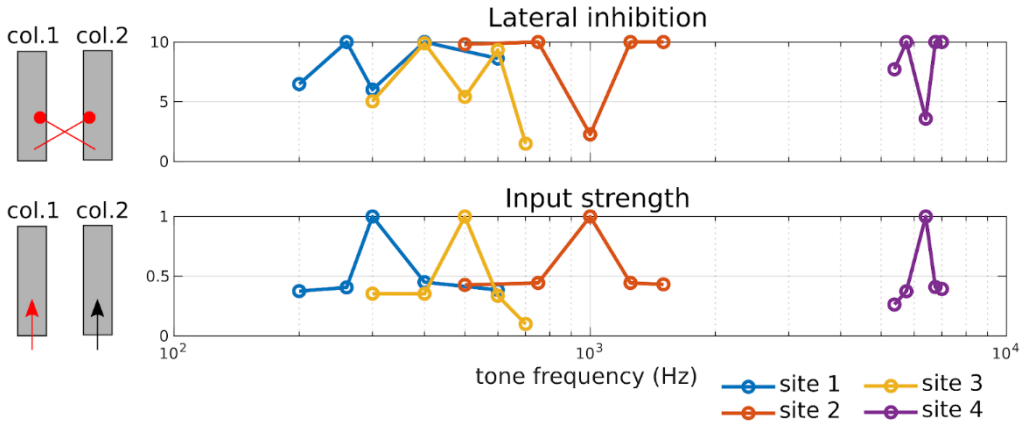

Figure 9. Lateral inhibition and input strength in evoked responses. The two fitted parameters are plotted against tone frequency (Hz in log scale). Lateral inhibition (represented by red lines with circle

749 *heads on the upper left) rescales default inter-column E2→SOM1 and E2→SOM2 connections. The*
750 *parameter input strength (represented by the red arrow on the bottom left) rescales the default input*
751 *strength of thalamic input Th→{E1, E2, E3, PV1, PV2} to Column 1 (representing the recording site).*
752 *Note that the input strength to Column 2 (representing the BF site) is always 1 and is not shown in*
753 *the plot. The fitted results for input strength are consistent with the tonotopic organization of A1,*
754 *showing peaks at the BFs (300, 1000, 500, and 6400 Hz) of the four recording sites. The fitted results*
755 *also suggest an M shape of lateral inhibition, with troughs occurring at the BFs of the recording sites*
756 *and maxima occurring at surrounding frequencies.*

757

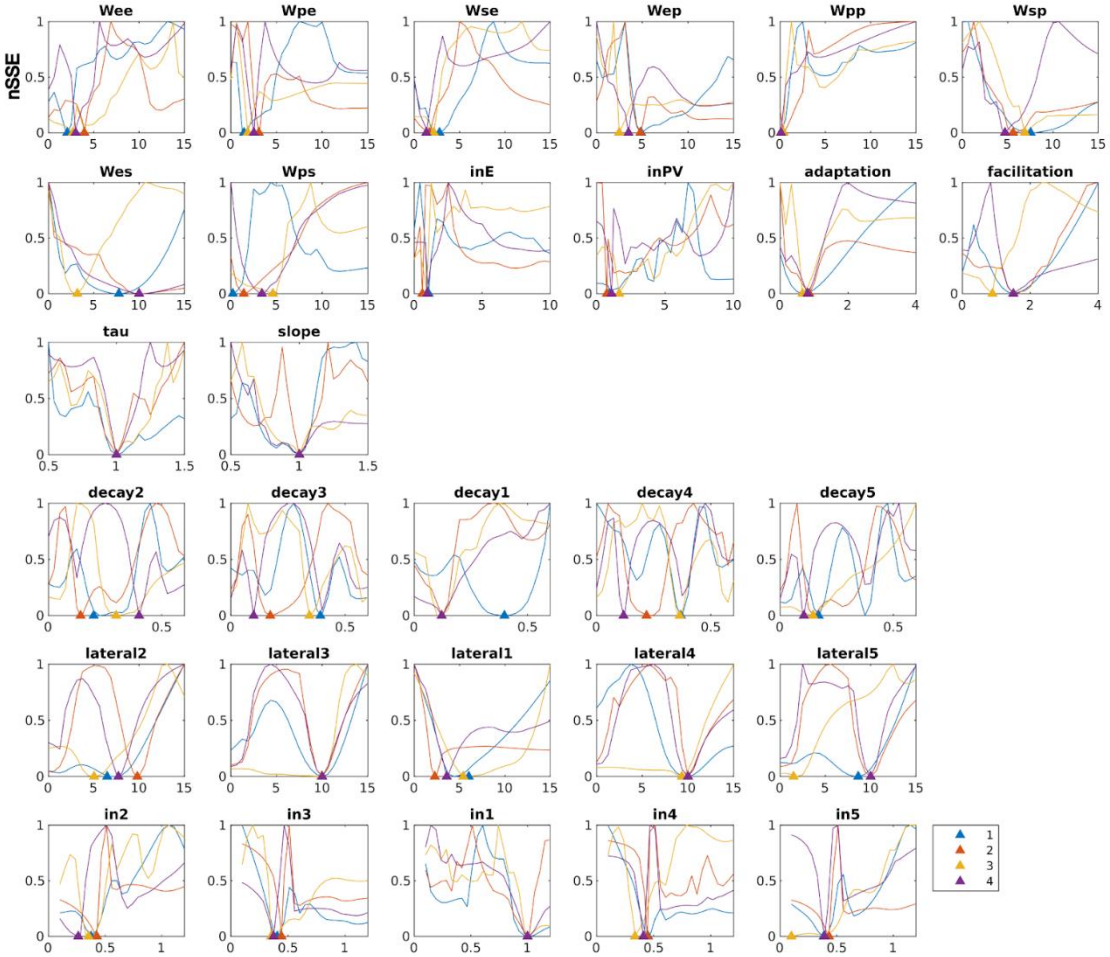

758 *Figure 10. Parameter sensitivity analysis. Axis parallel cuts through the cost function surfaces to target*

observations (i.e., sum of squared errors, SSE) of the four recording sites are normalized (nSSE) and shown in the color curves. The subplots contain the scanning on the 28 parameters (incl. W, InE, InPV, adaptation, facilitation, tau, slope, decay, lateral, and In2-5) and In1 (thalamic input under the BF condition, fixed to 1 during model fitting). The x-axis represents the scaling factors on default value 1. The triangles represent the solutions for the four recording sites.

4 Discussion

In this study, we combined a detailed neural circuit model of the cortex with fine-grained laminar LFP recordings in monkey primary auditory cortex (A1) to estimate cell-type specific contributions to both intracranially- and extracranially-recorded signals. We show that evoked responses at four example recording sites, covering a wide range in tonotopic space in A1, share similar network dynamics (i.e., E, PV, and SOM activity) (Figure 6), but can show diverse patterns in net transmembrane extracellular current flow, as reflected by CSD analysis, due to the variation in spatial profiles (Figure 8). The four recording sites also share similar input curves and lateral inhibition curves (Figure 9) as well as similar intra-column configurations (Figure 10). These results support the notion of canonical microcircuits and a consistent pattern of neural dynamics and interactions contributing to sensory processing in A1.

We demonstrate the feasibility of our model-fitting approach by transforming laminar profiles of MUA and CSD into products of spatial and temporal components. The fitted model provides insights into neural interactions and cell-type specific activities contributing to equivalent current dipoles (ECDs) underlying typical EEG or MEG recordings (Figure 7A). This is supported by the plausible ECD signal derived from the estimated current flows and CSD spatial profile. In contrast, an alternative approach based on non-negative matrix factorization, despite a higher goodness of fit to MUA and CSD

response profiles (Figure S2A), is relatively uninformative with regard to elucidating the activities of distinct neural populations (Figure S2B) and plausible synthesized ECD signals (Figure 7B).

4.1 PV-SOM interaction

We observed distinct patterns in the estimated activity of PV and SOM interneurons between BF and non-BF responses (Figure 6). In BF responses, PV interneurons show faster and stronger activity than SOM interneurons. In non-BF responses, PV interneurons show relatively weak activity, and the activity of SOM interneurons dominates after around 50 ms. This phenomenon results from various literature-based settings for PV and SOM neurons in the cortical column model with regard to thalamic input (no direct input to SOM), synaptic time constants (slow dynamic in SOM), inter-column connections (only E-to-SOM), and short-term plasticity (STF on E-to-SOM connections). In other words, the early PV activity is directly related to tonotopic (thalamic) input, and the late SOM activity is directly related to lateral inhibition. Based on this distinction, the switch between the “BF pattern” and “non-BF pattern” along the tonotopic axis is sharpened by mutual inhibition between PV and SOM interneurons (Hahn et al., 2022) and should be observable in possible future experiments involving detailed recordings from different neuron types, for example, through calcium imaging.

4.2 Generation of P1, N1, and P2 components

Auditory evoked responses recorded via EEG/MEG are typically characterized by a temporal sequence of positive and negative deflections or waves designated as the P1, N1, and P2 components. Studies based on the Human Neocortical Neurosolver (Kohl et al., 2022; Neymotin et al., 2020) suggest that the P1 and P2 components are partly generated by upward currents within the dendrites of cortical pyramidal neurons due to bottom-up inputs, while the N1 component is partly generated by downward currents associated with top-down inputs. Studies using a multi-column model of the auditory cortex (Hajizadeh et al., 2019, 2021, 2022) further emphasize the dependence

of current orientation on the cellular location of the active synapses (e.g., apical/somatic), synaptic type (i.e., excitatory/inhibitory), inter-column connection type (e.g., feedforward, feedback, within-field), and folding of the cortex (i.e., the neuroanatomical topography of the cortical surface). At the level of a cortical column, our analyses of the cell-specific contributions to ECDs (Figure 7A) suggests that initial thalamic input primarily contributes to P1, subsequent early activity of E and PV neurons (both BF and non-BF columns) primarily contributes to N1, and late SOM activity (especially in non-BF columns) joins the contribution to P2. We observed variability in peak latencies of the ECD signals at the four recording sites (Figure 7A), due to the variance in thalamic inputs, intra-column connection strengths, and the CSD laminar spatial profile across cortical columns.

4.3 Patterns of activity propagation

In this study, we were unable to identify a consistent pattern of neural activity propagation across cortical layers and neural populations contributing to the auditory evoked response. Such patterns (e.g., from L4 to L2/3 and to L5) have been assumed in canonical cortical column models of visual and somatosensory areas (e.g., (Douglas & Martin, 2004)). However, such a stereotypical pattern might not always be the rule. For example, a study using thalamic stimulation suggested that activity in supragranular layers is initiated by infragranular cells and regulated by feed-forward inhibitory cells (Krause et al., 2014). Moreover, specific patterns of information propagation are less likely to be found from a more detailed and complex network derived from existing animal-model databases (Billeh et al., 2020; Campagnola et al., 2022; Ji et al., 2016; Markram et al., 2015). Based on our estimated firing rates (Figure 6) and MUA spatial profile (Figure 8A), the three E populations (E1, E2, and E3) show early peaks at similar latencies because they all receive thalamic input. Clear propagation from L4 to L2/3 to L5 is therefore not observed. As for the activity of inhibitory neurons, PV1 activity is in general stronger than PV2 activity in BF responses, and SOM2 activity is stronger than SOM1 activity in non-BF responses. However, this pattern cannot be projected onto specific cortical layers, because

the estimated MUA spatial profiles of the same cell type (e.g., PV1 vs. PV2; SOM1 vs. SOM2) are not spatially exclusive. While our cortical column model was built with default connectivity based on laminar classification, the neural populations are found to spatially overlap after model fitting. Such spatial overlap of functional components may provide an alternative framework for understanding the neural computations underlying sensory processing, for example, the role of lateral inhibition in A1 in rhythmic masking release (Fishman et al., 2012), spectral resolution (Fishman & Steinschneider, 2006), and complex tone processing (Fishman et al., 2000b).

4.4 Limitations and future directions

Several important limitations of the present work should be noted. First, our model considers only thalamic and lateral input and disregards inputs from areas outside of primary auditory cortex, e.g., frontal and entorhinal cortices (Schaefer et al., 2015). Such input may be increasingly important for explaining neural activity occurring at longer latencies. Second, the firing rate in our model ranges from 0 to 1, corresponding to baseline activity and maximum firing rates of each cell type, respectively. We restricted the sigmoid functions to be non-negative in order to prevent unreasonable cancellation between negative and positive firing rates in the fitting procedure. This comes with the price of failing to explain negative (relative to the pre-stimulus baseline) MUA activity. Third, in order to avoid over-fitting, we reduced model complexity by making a number of simplifying assumptions. For example, the intra-column settings of the two columns are assumed to be identical. The ratio of thalamic input to E and PV neurons is assumed to be fixed. The inter-column connections are assumed to be symmetric. The MUA spatial profile is assumed to have a fixed ratio of sensitivity to E, PV, and SOM neurons. In general, these assumptions lead to a reduced goodness of fit. We cannot guarantee that we have found globally optimized solutions, but current best solutions show consistent neural activities and fitted parameters across the four recording sites examined. The current best solutions

can serve as a prior to improve goodness of fit to data from individual sites using a more flexible model, or one with a greater number of free parameters.

In this study, we demonstrated the feasibility of our model-fitting approach in estimating cell-type specific activity across cortical layers based on LFP recordings in A1. So far the target observations only include tone-evoked responses (BF and non-BF conditions) at four recording sites. Moreover, our cortical column model was designed with a relatively simple architecture in order to avoid an underdetermination issue arising from insufficient data constraints. However, our simplified model could be extended in several ways. For example, VIP interneurons could be included to examine the modulatory effects of attention on different inhibitory states (Hahn et al., 2022). The matrix thalamic input (innervating the supragranular cortex) could be included as tone-insensitive input (Müller et al., 2020) to investigate neural mechanisms underlying other neurophysiological phenomena in auditory cortex, such as “Off” responses and mismatch responses (e.g., (Fishman, 2014; Fishman & Steinschneider, 2009)). Corticothalamic pathways (which emanate from L5/6 to the thalamus) could also be included to model the modulation of thalamic input (Antunes & Malmierca, 2021). Lastly, spontaneous activity in LFP recordings could be considered in future work to examine the neural underpinnings of interactions between spontaneous and stimulus-evoked neural activity in auditory cortex (e.g., (Dura-Bernal et al., 2022)).

Acknowledgments

Neurophysiological data were obtained in collaboration with Dr. Mitchell Steinschneider (funded under NIH Grant DC00657), with invaluable technical support provided by Jeannie Hutagalung and Shirley Seto.

Supplementary figures

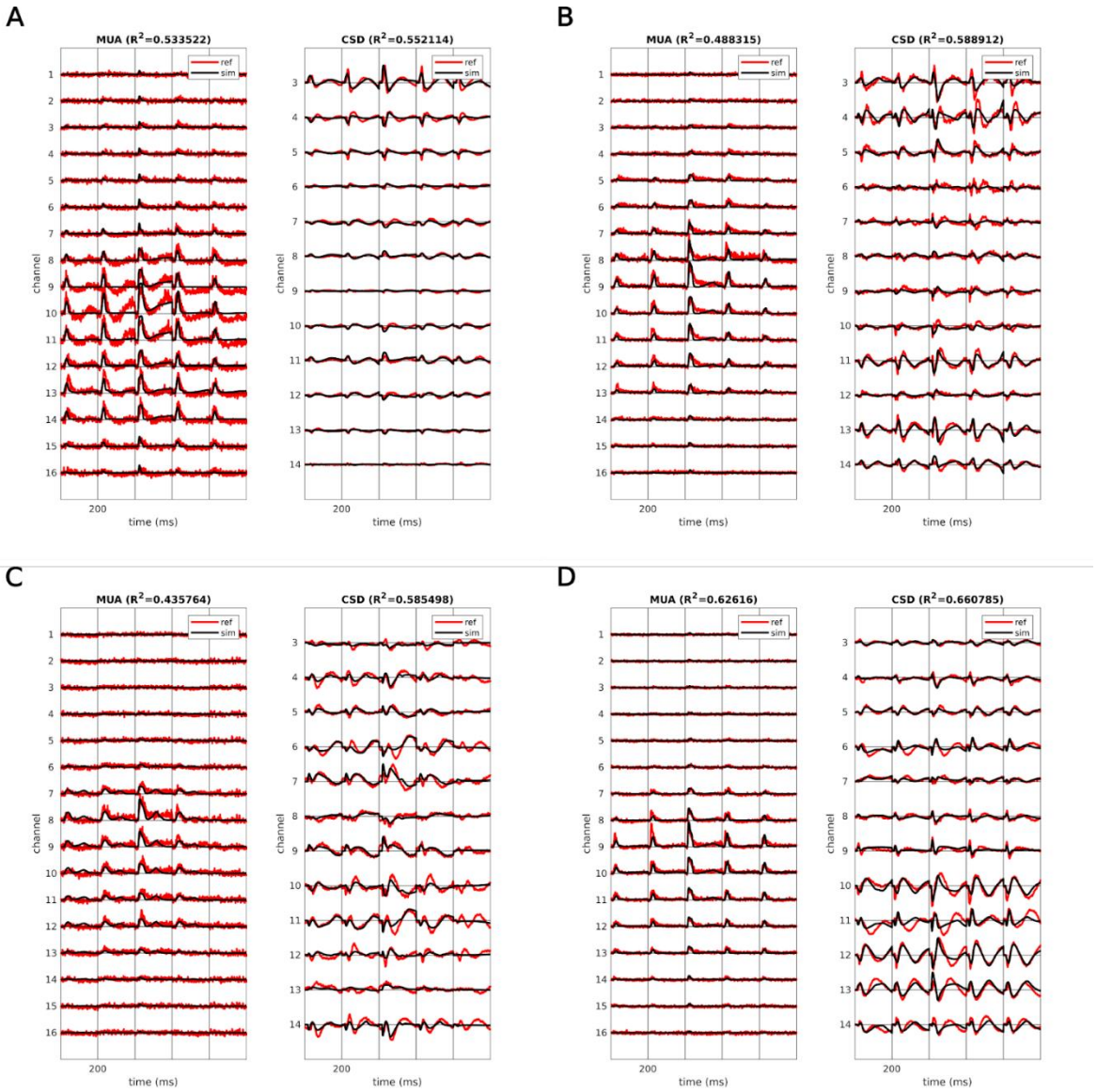

Figure S1. The goodness of fit, the target MUA and CSD (red), and the simulations (black) at sites 1 to 4 (A-D).

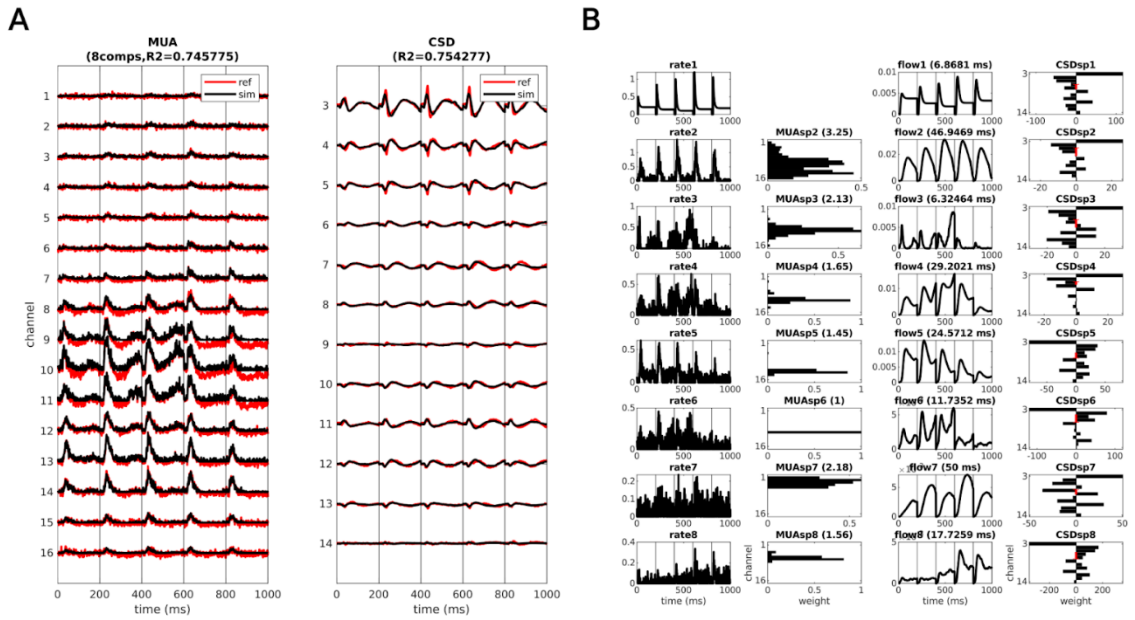

882 *Figure S2. The NNMF decomposition approach (site 1 used as example). (A) The goodness of fit, the*
883 *target MUA and CSD (red), and the model simulations (black). (B) The MUA is decomposed by NNMF*
884 *into firing rates (rates 2 to 8 in 1st column) and MUA spatial profile (2nd column). The thalamic input*
885 *(rate1 in 1st column) and the firing rates are convolved with alpha kernels to generate current flows*
886 *(3rd column). The CSD spatial profile is the regression coefficients, and the centers of sinks and*
887 *sources are shown in red arrows (4th column).*

888

References

Antunes, F. M., & Malmierca, M. S. (2021). Corticothalamic Pathways in Auditory Processing: Recent Advances and Insights From Other Sensory Systems. In *Frontiers in Neural Circuits* (Vol. 15). https://doi.org/10.3389/fncir.2021.721186

Aponte, D. A., Handy, G., Kline, A. M., Tsukano, H., Doiron, B., & Kato, H. K. (2021). Recurrent network dynamics shape direction selectivity in primary auditory cortex. *Nature Communications*, *12*(1). https://doi.org/10.1038/s41467-020-20590-6

Atencio, C. A., & Schreiner, C. E. (2013). Auditory cortical local subnetworks are characterized by sharply synchronous activity. *Journal of Neuroscience*, *33*(47). https://doi.org/10.1523/JNEUROSCI.2014-13.2013

Bacci, A., Rudolph, U., Huguenard, J. R., & Prince, D. A. (2003). Major Differences in Inhibitory Synaptic Transmission onto Two Neocortical Interneuron Subclasses. *Journal of Neuroscience*, *23*(29). https://doi.org/10.1523/jneurosci.23-29-09664.2003

Banno, T., Shirley, H. W., Fishman, Y. I., & Cohen, Y. E. (2022). Laminar Distribution of stimulus- and task-related variables related to auditory streaming in core and belt auditory cortex. *BioRxiv*, 2022.06.14.496098. https://doi.org/10.1101/2022.06.14.496098

Beierlein, M., Gibson, J. R., & Connors, B. W. (2003). Two Dynamically Distinct Inhibitory Networks in Layer 4 of the Neocortex. *Journal of Neurophysiology*, *90*(5). https://doi.org/10.1152/jn.00283.2003

Bigelow, J., Morrill, R. J., Dekloe, J., & Hasenstaub, A. R. (2019). Movement and VIP interneuron activation differentially modulate encoding in mouse auditory cortex. *ENeuro*, *6*(5). https://doi.org/10.1523/ENEURO.0164-19.2019

Billeh, Y. N., Cai, B., Gratiy, S. L., Dai, K., Iyer, R., Gouwens, N. W., Abbasi-Asl, R., Jia, X., Siegle, J. H., Olsen, S. R., Koch, C., Mihalas, S., & Arkhipov, A. (2020). Systematic Integration of Structural and Functional Data into Multi-scale Models of Mouse Primary Visual Cortex. *Neuron*, *106*(3). https://doi.org/10.1016/j.neuron.2020.01.040

Blackman, A. v., Abrahamsson, T., Costa, R. P., Lalanne, T., & Sjöström, P. J. (2013). Target-cell-specific short-term plasticity in local circuits. In *Frontiers in Synaptic Neuroscience* (Vol. 5, Issue DEC). https://doi.org/10.3389/fnsyn.2013.00011

Blackwell, J. M., & Geffen, M. N. (2017). Progress and challenges for understanding the function of cortical microcircuits in auditory processing. *Nature Communications*, *8*(1). https://doi.org/10.1038/s41467-017-01755-2

Brosch, M., Bauer, R., & Eckhorn, R. (1997). Stimulus-dependent modulations of correlated high-frequency oscillations in cat visual cortex. *Cerebral Cortex*, *7*(1). https://doi.org/10.1093/cercor/7.1.70

Bruyns-Haylett, M., Luo, J., Kennerley, A. J., Harris, S., Boorman, L., Milne, E., Vautrelle, N., Hayashi, Y., Whalley, B. J., Jones, M., Berwick, J., Riera, J., & Zheng, Y. (2017). The neurogenesis of P1 and

926 N1: A concurrent EEG/LFP study. *NeuroImage*, *146*.
927 https://doi.org/10.1016/j.neuroimage.2016.09.034
928 Campagnola, L., Seeman, S. C., Chartrand, T., Kim, L., Hoggarth, A., Gamlin, C., Ito, S., Trinh, J.,
929 Davoudian, P., Radaelli, C., Kim, M. H., Hage, T., Braun, T., Alfiler, L., Andrade, J., Bohn, P.,
930 Dalley, R., Henry, A., Kebede, S., … Jarsky, T. (2022). Local connectivity and synaptic dynamics in
931 mouse and human neocortex. *Science*, *375*(6585). https://doi.org/10.1126/science.abj5861
932 Chien, V. S. C., Maess, B., & Knösche, T. R. (2019). A generic deviance detection principle for cortical
933 On/Off responses, omission response, and mismatch negativity. *Biological Cybernetics*, *113*(5–
934 6). https://doi.org/10.1007/s00422-019-00804-x
935 Douglas, R. J., & Martin, K. A. C. (2004). Neuronal circuits of the neocortex. In *Annual Review of*
936 *Neuroscience* (Vol. 27). https://doi.org/10.1146/annurev.neuro.27.070203.144152
937 Dura-Bernal, S., Griffith, E. Y., Barczak, A., O'Connell, M. N., McGinnis, T., Schroeder, C. E., Lytton, W.
938 W., Lakatos, P., & Neymotin, S. A. (2022). Data-Driven Multiscale Model of Macaque Auditory
939 Thalamocortical Circuits Reproduces in vivo Dynamics. *SSRN Electronic Journal*.
940 https://doi.org/10.2139/ssrn.4219122
941 Einevoll, G. T., Pettersen, K. H., Devor, A., Ulbert, I., Halgren, E., & Dale, A. M. (2007). Laminar
942 population analysis: Estimating firing rates and evoked synaptic activity from multielectrode
943 recordings in rat barrel cortex. *Journal of Neurophysiology*, *97*(3).
944 https://doi.org/10.1152/jn.00845.2006
945 Fanselow, E. E., Richardson, K. A., & Connors, B. W. (2008). Selective, state-dependent activation of
946 somatostatin-expressing inhibitory interneurons in mouse neocortex. *Journal of*
947 *Neurophysiology*, *100*(5). https://doi.org/10.1152/jn.90691.2008
948 Fino, E., Packer, A. M., & Yuste, R. (2013). The logic of inhibitory connectivity in the neocortex. In
949 *Neuroscientist* (Vol. 19, Issue 3). https://doi.org/10.1177/1073858412456743
950 Fishman, Y. I. (2014). The mechanisms and meaning of the mismatch negativity. In *Brain Topography*
951 (Vol. 27, Issue 4). https://doi.org/10.1007/s10548-013-0337-3
952 Fishman, Y. I., Micheyl, C., & Steinschneider, M. (2012). Neural mechanisms of rhythmic masking
953 release in monkey primary auditory cortex: Implications for models of auditory scene analysis.
954 *Journal of Neurophysiology*, *107*(9). https://doi.org/10.1152/jn.01010.2011
955 Fishman, Y. I., Reser, D. H., Arezzo, J. C., & Steinschneider, M. (2000a). Complex tone processing in
956 primary auditory cortex of the awake monkey. I. Neural ensemble correlates of roughness. *The*
957 *Journal of the Acoustical Society of America*, *108*(1). https://doi.org/10.1121/1.429460
958 Fishman, Y. I., Reser, D. H., Arezzo, J. C., & Steinschneider, M. (2000b). Complex tone processing in
959 primary auditory cortex of the awake monkey. II. Pitch versus critical band representation. *The*
960 *Journal of the Acoustical Society of America*, *108*(1). https://doi.org/10.1121/1.429461
961 Fishman, Y. I., & Steinschneider, M. (2006). Spectral resolution of monkey primary auditory cortex
962 (A1) revealed with two-noise masking. *Journal of Neurophysiology*, *96*(3).
963 https://doi.org/10.1152/jn.00124.2006

964 Fishman, Y. I., & Steinschneider, M. (2009). Temporally dynamic frequency tuning of population
965 responses in monkey primary auditory cortex. *Hearing Research*, *254*(1–2).
966 https://doi.org/10.1016/j.heares.2009.04.010
967 Fishman, Y. I., & Steinschneider, M. (2010). Neural correlates of auditory scene analysis based on
968 inharmonicity in monkey primary auditory cortex. *Journal of Neuroscience*, *30*(37).
969 https://doi.org/10.1523/JNEUROSCI.1780-10.2010
970 Fishman, Y. I., & Steinschneider, M. (2012). Searching for the mismatch negativity in primary
971 auditory cortex of the awake monkey: Deviance detection or stimulus specific adaptation?
972 *Journal of Neuroscience*, *32*(45). https://doi.org/10.1523/JNEUROSCI.2835-12.2012
973 Fishman, Y. I., Volkov, I. O., Noh, M. D., Garell, P. C., Bakken, H., Arezzo, J. C., Howard, M. A., &
974 Steinschneider, M. (2001). Consonance and dissonance of musical chords: Neural correlates in
975 auditory cortex of monkeys and humans. *Journal of Neurophysiology*, *86*(6).
976 https://doi.org/10.1152/jn.2001.86.6.2761
977 Freeman, J. A., & Nicholson, C. (1975). Experimental optimization of current source density
978 technique for anuran cerebellum. *Journal of Neurophysiology*, *38*(2).
979 https://doi.org/10.1152/jn.1975.38.2.369
980 Głąbska, H., Potworowski, J., Łęski, S., & Wójcik, D. K. (2014). Independent components of neural
981 activity carry information on individual populations. *PLoS ONE*, *9*(8).
982 https://doi.org/10.1371/journal.pone.0105071
983 Głąbska, H. T., Norheim, E., Devor, A., Dale, A. M., Einevoll, G. T., & Wójcik, D. K. (2016). Generalized
984 laminar population analysis (gLPA) for interpretation of multielectrode data from cortex.
985 *Frontiers in Neuroinformatics*, *10*(JAN). https://doi.org/10.3389/fninf.2016.00001
986 Hagen, E., Dahmen, D., Stavrinou, M. L., Lindén, H., Tetzlaff, T., van Albada, S. J., Grün, S., Diesmann,
987 M., & Einevoll, G. T. (2016). Hybrid scheme for modeling local field potentials from point-
988 neuron networks. *Cerebral Cortex*, *26*(12). https://doi.org/10.1093/cercor/bhw237
989 Hagen, E., Næss, S., Ness, T. v., & Einevoll, G. T. (2018). Multimodal modeling of neural network
990 activity: Computing LFP, ECoG, EEG, and MEG signals with LFPy 2.0. *Frontiers in*
991 *Neuroinformatics*, *12*. https://doi.org/10.3389/fninf.2018.00092
992 Hahn, G., Kumar, A., Schmidt, H., Knösche, T. R., & Deco, G. (2022). Rate and oscillatory switching
993 dynamics of a multilayer visual microcircuit model. *ELife*, *11*, e77594.
994 https://doi.org/10.7554/eLife.77594
995 Hajizadeh, A., Matysiak, A., Brechmann, A., König, R., & May, P. J. C. (2021). Why do humans have
996 unique auditory event-related fields? Evidence from computational modeling and MEG
997 experiments. *Psychophysiology*, *58*(4). https://doi.org/10.1111/psyp.13769
998 Hajizadeh, A., Matysiak, A., May, P. J. C., & König, R. (2019). Explaining event-related fields by a
999 mechanistic model encapsulating the anatomical structure of auditory cortex. *Biological*
1000 *Cybernetics*, *113*(3). https://doi.org/10.1007/s00422-019-00795-9
1001 Hajizadeh, A., Matysiak, A., Wolfrum, M., May, P. J. C., & König, R. (2022). Auditory cortex modelled

as a dynamical network of oscillators: understanding event-related fields and their adaptation. *Biological Cybernetics*, *116*(4), 475–499. https://doi.org/10.1007/s00422-022-00936-7

Hamilton, L. S., Sohl-Dickstein, J., Huth, A. G., Carels, V. M., Deisseroth, K., & Bao, S. (2013). Optogenetic Activation of an Inhibitory Network Enhances Feedforward Functional Connectivity in Auditory Cortex. *Neuron*, *80*(4). https://doi.org/10.1016/j.neuron.2013.08.017

Happel, M. F. K., Jeschke, M., & Ohl, F. W. (2010). Spectral integration in primary auditory cortex attributable to temporally precise convergence of thalamocortical and intracortical input. *Journal of Neuroscience*, *30*(33). https://doi.org/10.1523/JNEUROSCI.0689-10.2010

Hayut, I., Fanselow, E. E., Connors, B. W., & Golomb, D. (2011). LTS and FS inhibitory interneurons, short-term synaptic plasticity, and cortical circuit dynamics. *PLoS Computational Biology*, *7*(10). https://doi.org/10.1371/journal.pcbi.1002248

Jansen, B. H., & Rit, V. G. (1995). Electroencephalogram and visual evoked potential generation in a mathematical model of coupled cortical columns. *Biological Cybernetics*, *73*(4). https://doi.org/10.1007/BF00199471

Ji, X. Y., Zingg, B., Mesik, L., Xiao, Z., Zhang, L. I., & Tao, H. W. (2016). Thalamocortical Innervation Pattern in Mouse Auditory and Visual Cortex: Laminar and Cell-Type Specificity. *Cerebral Cortex*, *26*(6). https://doi.org/10.1093/cercor/bhv099

Jouhanneau, J. S., Kremkow, J., & Poulet, J. F. A. (2018). Single synaptic inputs drive high-precision action potentials in parvalbumin expressing GABA-ergic cortical neurons in vivo. *Nature Communications*, *9*(1). https://doi.org/10.1038/s41467-018-03995-2

Kaas, J. H., & Hackett, T. A. (2000). Subdivisions of auditory cortex and processing streams in primates. In *Proceedings of the National Academy of Sciences of the United States of America* (Vol. 97, Issue 22). https://doi.org/10.1073/pnas.97.22.11793

Kayser, C., Petkov, C. I., & Logothetis, N. K. (2007). Tuning to sound frequency in auditory field potentials. *Journal of Neurophysiology*, *98*(3). https://doi.org/10.1152/jn.00358.2007

Keller, D., Erö, C., & Markram, H. (2018). Cell densities in the mouse brain: A systematic review. In *Frontiers in Neuroanatomy* (Vol. 12). https://doi.org/10.3389/fnana.2018.00083

Kohl, C., Parviainen, T., & Jones, S. R. (2022). Neural Mechanisms Underlying Human Auditory Evoked Responses Revealed By Human Neocortical Neurosolver. *Brain Topography*, *35*(1). https://doi.org/10.1007/s10548-021-00838-0

Krause, B. M., Raz, A., Uhlrich, D. J., Smith, P. H., & Banks, M. I. (2014). Spiking in auditory cortex following thalamic stimulation is dominated by cortical network activity. *Frontiers in Systems Neuroscience*, *8*. https://doi.org/10.3389/fnsys.2014.00170

Kunze, T., Haueisen, J., & Knösche, T. R. (2019). Emergence of cognitive priming and structure building from the hierarchical interaction of canonical microcircuit models. *Biological Cybernetics*, *113*(3), 273–291. https://doi.org/10.1007/s00422-019-00792-y

Lakatos, P., O'Connell, M. N., Barczak, A., McGinnis, T., Neymotin, S., Schroeder, C. E., Smiley, J. F., & Javitt, D. C. (2020). The Thalamocortical Circuit of Auditory Mismatch Negativity. *Biological*

Psychiatry, *87*(8). https://doi.org/10.1016/j.biopsych.2019.10.029

Liu, J., & Kanold, P. O. (2021). Diversity of receptive fields and sideband inhibition with complex thalamocortical and intracortical origin in L2/3 of mouse primary auditory cortex. *Journal of Neuroscience*, *41*(14). https://doi.org/10.1523/JNEUROSCI.1732-20.2021

Liu, J., Whiteway, M. R., Sheikhattar, A., Butts, D. A., Babadi, B., & Kanold, P. O. (2019). Parallel Processing of Sound Dynamics across Mouse Auditory Cortex via Spatially Patterned Thalamic Inputs and Distinct Areal Intracortical Circuits. *Cell Reports*, *27*(3). https://doi.org/10.1016/j.celrep.2019.03.069

Lopes da Silva, F. (2013). EEG and MEG: Relevance to Neuroscience. *Neuron*, *80*(5), 1112–1128. https://doi.org/10.1016/J.NEURON.2013.10.017

Ma, Y., Hu, H., & Agmon, A. (2012). Short-term plasticity of unitary inhibitory-to-inhibitory synapses depends on the presynaptic interneuron subtype. *Journal of Neuroscience*, *32*(3). https://doi.org/10.1523/JNEUROSCI.5007-11.2012

Markram, H., Muller, E., Ramaswamy, S., Reimann, M. W., Abdellah, M., Sanchez, C. A., Ailamaki, A., Alonso-Nanclares, L., Antille, N., Arsever, S., Kahou, G. A. A., Berger, T. K., Bilgili, A., Buncic, N., Chalimourda, A., Chindemi, G., Courcol, J. D., Delalondre, F., Delattre, V., … Schürmann, F. (2015). Reconstruction and Simulation of Neocortical Microcircuitry. *Cell*, *163*(2). https://doi.org/10.1016/j.cell.2015.09.029

Merzenich, M. M., & Brugge, J. F. (1973). Representation of the cochlear partition on the superior temporal plane of the macaque monkey. *Brain Research*, *50*(2). https://doi.org/10.1016/0006-8993(73)90731-2

Mesik, L., Ma, W. P., Li, L. Y., Ibrahim, L. A., Huang, Z. J., Zhang, L., & Tao, H. W. (2015). Functional response properties of VIP-expressing inhibitory neurons in mouse visual and auditory cortex. *Frontiers in Neural Circuits*, *9*(May). https://doi.org/10.3389/fncir.2015.00022

Metherate, R., & Cruikshank, S. J. (1999). Thalamocortical inputs trigger a propagating envelope of gamma-band activity in auditory cortex in vitro. *Experimental Brain Research*, *126*(2). https://doi.org/10.1007/s002210050726

Morel, A., Garraghty, P. E., & Kaas, J. H. (1993). Tonotopic organization, architectonic fields, and connections of auditory cortex in macaque monkeys. *Journal of Comparative Neurology*, *335*(3). https://doi.org/10.1002/cne.903350312

Müller, E. J., Munn, B., Hearne, L. J., Smith, J. B., Fulcher, B., Arnatkevičiūtė, A., Lurie, D. J., Cocchi, L., & Shine, J. M. (2020). Core and matrix thalamic sub-populations relate to spatio-temporal cortical connectivity gradients. *NeuroImage*, *222*. https://doi.org/10.1016/j.neuroimage.2020.117224

Müller-Preuss, P., & Mitzdorf, U. (1984). Functional anatomy of the inferior colliculus and the auditory cortex: current source density analyses of click-evoked potentials. *Hearing Research*, *16*(2). https://doi.org/10.1016/0378-5955(84)90003-0

Næss, S., Halnes, G., Hagen, E., Hagler, D. J., Dale, A. M., Einevoll, G. T., & Ness, T. v. (2021).

Biophysically detailed forward modeling of the neural origin of EEG and MEG signals. *NeuroImage*, *225*. https://doi.org/10.1016/j.neuroimage.2020.117467

Neymotin, S. A., Daniels, D. S., Caldwell, B., McDougal, R. A., Carnevale, N. T., Jas, M., Moore, C. I., Hines, M. L., Hämäläinen, M., & Jones, S. R. (2020). Human neocortical neurosolver (HNN), a new software tool for interpreting the cellular and network origin of human MEG/EEG data. *ELife*, *9*. https://doi.org/10.7554/eLife.51214

Nicholson, C., & Freeman, J. A. (1975). Theory of current source density analysis and determination of conductivity tensor for anuran cerebellum. *Journal of Neurophysiology*, *38*(2). https://doi.org/10.1152/jn.1975.38.2.356

O'Connell, M. N., Falchier, A., McGinnis, T., Schroeder, C. E., & Lakatos, P. (2011). Dual Mechanism of Neuronal Ensemble Inhibition in Primary Auditory Cortex. *Neuron*, *69*(4). https://doi.org/10.1016/j.neuron.2011.01.012

Park, Y., & Geffen, M. N. (2020). A circuit model of auditory cortex. *PLoS Computational Biology*, *16*(7). https://doi.org/10.1371/journal.pcbi.1008016

Pérez-González, D., & Malmierca, M. S. (2014). Adaptation in the auditory system: An overview. In *Frontiers in Integrative Neuroscience* (Vol. 8, Issue FEB). https://doi.org/10.3389/fnint.2014.00019

Regehr, W. G. (2012). Short-Term Presynaptic Plasticity. *Cold Spring Harbor Perspectives in Biology*, *4*(7), 1–19. https://doi.org/10.1101/CSHPERSPECT.A005702

Schaefer, M. K., Hechavarría, J. C., & Kössl, M. (2015). Quantification of mid and late evoked sinks in laminar current source density profiles of columns in the primary auditory cortex. *Frontiers in Neural Circuits*, *9*(OCT). https://doi.org/10.3389/fncir.2015.00052

Schroeder, C. E., Mehta, A. D., & Givre, S. J. (1998). A spatiotemporal profile of visual system activation revealed by current source density analysis in the awake macaque. *Cerebral Cortex*, *8*(7). https://doi.org/10.1093/cercor/8.7.575

Silberberg, G., Grillner, S., LeBeau, F. E. N., Maex, R., & Markram, H. (2005). Synaptic pathways in neural microcircuits. In *Trends in Neurosciences* (Vol. 28, Issue 10). https://doi.org/10.1016/j.tins.2005.08.004

Silberberg, G., & Markram, H. (2007). Disynaptic Inhibition between Neocortical Pyramidal Cells Mediated by Martinotti Cells. *Neuron*, *53*(5). https://doi.org/10.1016/j.neuron.2007.02.012

Steinschneider, M., Fishman, Y. I., & Arezzo, J. C. (2003). Representation of the voice onset time (VOT) speech parameter in population responses within primary auditory cortex of the awake monkey. *The Journal of the Acoustical Society of America*, *114*(1). https://doi.org/10.1121/1.1582449

Steinschneider, M., Reser, D. H., Fishman, Y. I., Schroeder, C. E., & Arezzo, J. C. (1998). Click train encoding in primary auditory cortex of the awake monkey: Evidence for two mechanisms subserving pitch perception. *The Journal of the Acoustical Society of America*, *104*(5). https://doi.org/10.1121/1.423877

Steinschneider, M., Schroeder, C. E., Arezzo, J. C., & Vaughan, H. G. (1994). Speech-evoked activity in primary auditory cortex: effects of voice onset time. *Electroencephalography and Clinical Neurophysiology/ Evoked Potentials*, *92*(1). https://doi.org/10.1016/0168-5597(94)90005-1

Steinschneider, M., Tenke, C. E., Schroeder, C. E., Javitt, D. C., Simpson, G. v., Arezzo, J. C., & Vaughan, H. G. (1992). Cellular generators of the cortical auditory evoked potential initial component. *Electroencephalography and Clinical Neurophysiology/ Evoked Potentials*, *84*(2). https://doi.org/10.1016/0168-5597(92)90026-8

Studer, F., & Barkat, T. R. (2022). Inhibition in the auditory cortex. In *Neuroscience and Biobehavioral Reviews* (Vol. 132). https://doi.org/10.1016/j.neubiorev.2021.11.021

Sukov, W., & Barth, D. S. (1998). Three-dimensional analysis of spontaneous and thalamically evoked gamma oscillations in auditory cortex. *Journal of Neurophysiology*, *79*(6). https://doi.org/10.1152/jn.1998.79.6.2875

Sumner, R. L., Spriggs, M. J., & Shaw, A. D. (2021). Modelling thalamocortical circuitry shows that visually induced LTP changes laminar connectivity in human visual cortex. *PLoS Computational Biology*, *17*(1). https://doi.org/10.1371/journal.pcbi.1008414

Supèr, H., & Roelfsema, P. R. (2005). Chronic multiunit recordings in behaving animals: Advantages and limitations. In *Progress in Brain Research* (Vol. 147, Issue SPEC. ISS.). https://doi.org/10.1016/S0079-6123(04)47020-4

Tenke, C. E., & Kayser, J. (2012). Generator localization by current source density (CSD): Implications of volume conduction and field closure at intracranial and scalp resolutions. In *Clinical Neurophysiology* (Vol. 123, Issue 12). https://doi.org/10.1016/j.clinph.2012.06.005

Vaughan H.G.Jr. (1988). The neural basis of event-related potentials. *Human Event-Related Potentials*, 45–96. http://ci.nii.ac.jp/naid/10008963195/ja/

Wang, P., & Knösche, T. R. (2013). A realistic neural mass model of the cortex with laminar-specific connections and synaptic plasticity - evaluation with auditory habituation. *PloS One*, *8*(10). https://doi.org/10.1371/journal.pone.0077876

Wang, P., Kong, R., Kong, X., Liégeois, R., Orban, C., Deco, G., van den Heuvel, M. P., & Yeo, B. T. T. (2019). Inversion of a large-scale circuit model reveals a cortical hierarchy in the dynamic resting human brain. *Tropical and Subtropical Agroecosystems*, *21*(3). https://doi.org/10.1126/sciadv.aat7854